Monthly Notices of the ROYAL ASTRONOMICAL SOCIETY

MNRAS **504,** 928–950 (2021) doi:10.1093/mnras/stab674
Advance Access publication 2021 March 8

Unveiling the nature of 11 dusty star-forming galaxies at the peak of cosmic star formation history

L. Pantoni,[1,2★] A. Lapi,[1,2,3,4] M. Massardi,[5] D. Donevski,[1,3] A. Bressan,[1] L. Silva,[4] F. Pozzi,[6,7] C. Vignali,[6,7] M. Talia,[6,7] A. Cimatti,[6,8] T. Ronconi[1,2,3] and L. Danese[1,3]

[1]*SISSA – ISAS, Via Bonomea 265, I-34136 Trieste, Italy*
[2]*INFN – Sezione di Trieste, via Valerio 2, I-34127 Trieste, Italy*
[3]*IFPU – Institute for fundamental physics of the Universe, Via Beirut 2, I-34014 Trieste, Italy*
[4]*INAF – Osservatorio Astronomico di Trieste, Via Giambattista Tiepolo, 11, I-34131 Trieste, Italy*
[5]*INAF – Istituto di Radioastronomia – Italian ARC, Via Piero Gobetti 101, I-40129 Bologna, Italy*
[6]*DIFA – Dipartimento di Fisica e Astronomia, Università degli Studi di Bologna, Via Berti Pichat 6/2, I-40127 Bologna, Italy*
[7]*INAF – Osservatorio di Astrofisica e Scienza dello Spazio di Bologna, Via Gobetti 93/3, I-40129 Bologna, Italy*
[8]*INAF – Osservatorio Astrofisico di Arcetri, Largo E. Fermi, I-50125 Firenze, Italy*

Accepted 2021 March 2. Received 2021 February 8; in original form 2020 November 12

ABSTRACT

We present a panchromatic study of 11 (sub-)millimetre selected DSFGs with spectroscopically confirmed redshift ($1.5 < z_{\rm spec} < 3$) in the GOODS-S field, with the aim of constraining their astrophysical properties (e.g. age, stellar mass, dust, and gas content) and characterizing their role in the context of galaxy evolution. The multiwavelength coverage of GOODS-S, from X-rays to radio band, allow us to model galaxy SED by using CIGALE z with a novel approach, based on a physical motivated modelling of stellar light attenuation by dust. Median stellar mass ($\simeq 6.5 \times 10^{10}$ M$_\odot$) and SFR ($\simeq 241$ M$_\odot$ yr^{-1}) are consistent with galaxy main sequence at $z \sim 2$. The galaxies are experiencing an intense and dusty burst of star formation (median $L_{\rm IR} \simeq 2 \times 10^{12}$ $L_\odot$), with a median age of 750 Myr. The high median content of interstellar dust ($M_{\rm dust} \simeq 5 \times 10^8$ M$_\odot$) suggests a rapid enrichment of the ISM (on time-scales $\sim 10^8$ yr). We derived galaxy total and molecular gas content from CO spectroscopy and/or Rayleigh–Jeans dust continuum ($10^{10} \lesssim M_{\rm gas}/{\rm M}_\odot \lesssim 10^{11}$), depleted over a typical time-scale $\tau_{\rm depl} \sim 200$ Myr. X-ray and radio luminosities ($L_{\rm X} = 10^{42}$–10^{44} erg s^{-1}, $L_{1.5\,{\rm GHz}} = 10^{30}$–$10^{31}$ erg s^{-1}, $L_{6\,{\rm GHz}} = 10^{29}$–$10^{30}$ erg s^{-1}) suggest that most of the galaxies hosts an accreting radio-silent/quiet SMBH. This evidence, along with their compact multiwavelength sizes (median $r_{\rm ALMA} \sim r_{\rm VLA} = 1.8$ kpc, $r_{HST} = 2.3$ kpc) measured from high-resolution imaging ($\theta_{\rm res} \lesssim 1$ arcsec), indicates these objects as the high-z star-forming counterparts of massive quiescent galaxies, as predicted e.g. by the *in situ* scenario. Four objects show some signatures of a forthcoming/ongoing AGN feedback, which is thought to trigger the morphological transition from star-forming discs to ETGs.

Key words: galaxies: evolution – galaxies: high-redshift – galaxies: photometry – galaxies: star formation – infrared: galaxies – submillimetre: galaxies.

1 INTRODUCTION

Dusty star-forming galaxies (DSFGs) have been discovered almost 20 yr ago as an abundant population of distant galaxies characterized by a 850-μm flux density greater than a few mJy (e.g. Blain et al. 2002; Hodge et al. 2013; Casey, Narayanan & Cooray 2014; da Cunha et al. 2015; Miettinen et al. 2015; Simpson et al. 2015; Oteo et al. 2016). The subsequent multiwavelength campaigns (e.g. Hubble Ultra Deep Field, HUDF, Beckwith et al. 2006), along with deep and large-area blind surveys in the infrared domain, e.g. PACS Evolutionary Probe, PEP (Lutz et al. 2011), *Herschel* Multi-tired Extra-galactic Survey, HerMES (Oliver et al. 2012), Astrophysical Terahertz Large Area Survey, H-ATLAS (Eales et al. 2010), revealed their nature as massive and very infrared luminous galaxies (with typical stellar mass $M_\star \sim$ a few 10^{10}–10^{11} M$_\odot$ and infrared luminosity $L_{\rm IR} \sim 10^{11}$–10^{12} $L_\odot$), characterized by extreme star formation rates (SFRs > 100 M$_\odot$ yr^{-1}; e.g. Gruppioni et al. 2013; Béthermin et al. 2017). Due to the intense star formation and the rapid dust enrichment of the interstellar medium (ISM), these objects are usually very faint or invisible in the UV/optical domains (even where maps to very low flux density level are available), since dust obscuration is very efficient in these spectral regimes (e.g. Smail et al. 1999; Walter et al. 2012; Franco et al. 2018; Williams et al. 2019). In the millimetre band, the cosmological dimming affecting high-z sources is actually offset for these dusty objects by the shifting of the dust peak into the observing band (the so-called *negative k-correction*). As a result, the flux density remains almost constant over a large redshift range, i.e. $z \sim 1$–10.

The first spectroscopic follow-up campaigns revealed their number density to peak at redshift $\sim$2.5 (Chapman et al. 2003, 2005), which is almost coincident with the peak of Cosmic star formation history (Cosmic SFH; see the review by Madau & Dickinson 2014) and black hole accretion history (BHAH; e.g. Shankar, Weinberg & Miralda-

★ E-mail: lpantoni@sissa.it

Escudé 2009; Aird et al. 2010; Delvecchio et al. 2014). On the one hand, DSFGs contribute significantly to both the Cosmic star formation rate density (Cosmic SFRD) and the stellar mass density, supplying, respectively, with the ∼20 and ∼30–50 per cent at z = 2–4 (see e.g. Michałowski, Hjorth & Watson 2010). On the other hand, they possibly assume a central role in the evolution of active galactic nuclei (AGNs) and ultimately in the building up of compact quiescient galaxies and massive, local early-type galaxies (ETGs; see e.g. Swinbank et al. 2006; Cimatti et al. 2008; van Dokkum et al. 2008; Barro et al. 2013; Simpson et al. 2014; Toft et al. 2014; Oteo et al. 2017; Scoville et al. 2017)

For these reasons, high-z DSFGs represent a crucial tool to solve the complex puzzles of stellar mass assembly and massive galaxies evolution out to $z > 3$ (e.g. Gruppioni et al. 2020; Talia et al. 2020). Although many progresses have been made in the recent few years, in particular with the advent of ALMA (see the review by Hodge & da Cunha 2020), we are far away from fully physically characterizing this class of galaxies and from thoroughly understanding their role in the framework of galaxy formation and evolution.

In order to address these issues, two different (and complementary) approaches are currently on the market, both exploiting the wealth of data recently collected by the numerous wide-area and deep multiband surveys.

The first approach aims at constraining one (or a few) specific property of the galaxy population (e.g. stellar mass, dust mass, attenuation, metallicity, environment), relying on the analysis of statistically significant samples of DSFGs (see e.g. Béthermin et al. 2014; da Cunha et al. 2015; Casey et al. 2018; Donevski et al. 2018; Franco et al. 2018; Pearson et al. 2018). The analysis is often built on a few well-sampled spectral bands (e.g. Magdis et al. 2012; Małek et al. 2018), while just in some cases it is multimessenger (e.g. Pearson et al. 2018; Buat et al. 2019; Donevski et al. 2020). To preserve the statistical relevance of the outcomes, this approach extensively exploits e.g. the building of synthesized spectral energy distributions (SEDs), especially when the sampling is not uniform for every objects (e.g. Bianchini et al. 2019), and the analysis of stacked data (e.g. Santini et al. 2014; Scoville et al. 2016). Indeed, one of the main drawbacks of this approach is the incompleteness of the data: The available information (e.g. observed frequency, sensitivity, redshift) is typically not homogeneous over the whole sample. In addition, the outcomes may suffer from some selection-bias (depending on the survey exploited to collect the data) and could be affected by uncertainties due to the exploitation of photometric redshift and, eventually, by assumptions on galaxy undersampled properties.

The second approach focuses on the analysis of small samples or individual objects with a huge number of quality data (both photometric and spectroscopic), with the aim of gaining a deep insight on the ongoing astrophysical processes. Typically, this objective is reached by exploiting high-resolution imaging (usually in the millimetre and radio regimes) and spectral-line analysis, which provide an almost secure determination of galaxy spectroscopic redshift, kinematics, and size (e.g. Tadaki et al. 2015; Decarli et al. 2016; Barro et al. 2016a, b; Talia et al. 2018). At high-z, this analysis requires very long integration times (i.e. orders of a few hours) that do not allow the method to be applied to statistical samples. Some studies partially overcome this problem by focusing on gravitationally lensed objects (e.g. Negrello et al. 2014; Massardi et al. 2018; Stacey et al. 2020), even if this strategy requires to model the foreground lens in order to obtain the *original* (i.e. unbent) image of the target galaxy. Although the outcomes do not have any statistical relevance for the whole population of DSFGs, their accuracy can provide an exquisite characterization of the individual object, which encompasses all the galaxy properties, when complemented with the wealth of multiwavelength photometry currently available (see e.g. Rujopakarn et al. 2016; Elbaz et al. 2018).

In this work, we follow the latter approach focusing on a sample of 11 spectroscopically confirmed $z \sim 2$ DSFGs, which we selected in the Great Observatories Origins Survey South (GOODS-S; Dickinson & GOODS Legacy Team 2001; Giavalisco et al. 2004) field, in order to have the widest multiwavelength coverage of their spectral/broad-band emission currently achievable (from X-rays to radio band). Such accurate sampling is fundamental to derive galaxy astrophysical properties, since their SED is the outcome of all the complex processes occurring between the diverse baryonic components, such as stars and their remnants, cold and warm gas, interstellar dust, and central SMBH. We complement the photometric data with high-resolution imaging ($\theta_{\rm res} \lesssim 1$ arcsec), providing information on galaxy morphology and multiband sizes, which have been recognized to have a crucial role in studying galaxy formation and evolution (see e.g. Lapi et al. 2018). We stress that such a panchromatic approach, combining the outcomes from SED analysis with galaxy spectroscopy and high-resolution imaging, is essential to unbiasedly extract information from multiband data and shed light on galaxy evolution.

Our main goal is to provide a pilot work on a spectroscopically confirmed sample of DSFGs at the peak of Cosmic SFH that presents a detailed analysis of the interplay between the ongoing astrophysical processes (such as gas condensation, star formation, central BH accretion, and feedback) and a consistent interpretative picture in the framework of galaxy evolution, by exploiting the multiple information coming from photometry, spectroscopy, and imaging at high resolution. Such a novel approach, which easily applies to our small sample of galaxies, could be extended to other multiband fields (e.g. COSMOS and H-ATLAS; see e.g. Neri et al. 2020) and exploited for studying future big samples of spectroscopically confirmed DSFGs with multiband follow-up (see e.g. the ongoing z-GAL NOEMA Large Program[1]; PIs: P. Cox; T. Bakx; H.Dannerbauer).

This paper is organized as follows. In Section 2, we describe the selection criteria we use to build our sample of 11 DSFGs and list the multiwavelength data available for each source; in Section 3, we describe the method we follow to model galaxy SEDs, while in Section 4, we illustrate the corresponding outcomes and match the results with other evidences coming from the available spectral lines and high-resolution imaging; in Section 5, we discuss our results by referring to the *in situ* BH-galaxy co-evolution scenario (see Mancuso et al. 2016b, 2017; Lapi et al. 2018; Pantoni et al. 2019), and compare our findings with other recent studies on high-z DSFGs. In Section 6, we summarize the main outcomes of the present work and we outline our conclusions.

Throughout this work, we adopt the standard flat ΛCDM cosmology (Planck Collaboration VI 2020) with rounded parameter values: matter density $\Omega_{\rm M} = 0.32$, dark energy density $\Omega_\Lambda = 0.63$, baryon density $\Omega_{\rm b} = 0.05$, Hubble constant $H_0 = 100\,h$ km s^{-1} Mpc^{-1} with $h = 0.67$, and mass variance $\sigma_8 = 0.81$ on a scale of 8 h^{-1} Mpc.

2 THE SAMPLE

In order to reach our basic goal, i.e. the accurate sampling of galaxy SED from the X-ray to the radio band, we selected our sample of high-z DSFGs in the (sub-)millimetre regime requiring the following criteria to be fulfilled for each galaxy: three or more detections in

[1] http://www.iram.fr/z-gal/Home.htm.

Table 1. The 11 (sub-)millimetre sources of our sample.

ID∗	ID∗∗	$z_{\rm spec}$	$\rm RA_{ALMA}$ ($^{\rm h}$:$^{\rm m}$:$^{\rm s}$)	$\rm Dec._{ALMA}$ ($^\circ$:$'$:$''$)	$\rm RA_{\textit{HST}}$ ($^{\rm h}$:$^{\rm m}$:$^{\rm s}$)	$\rm Dec._{\textit{HST}}$ ($^\circ$:$'$:$''$)	$\rm RA_{mm}$ ($^{\rm h}$:$^{\rm m}$:$^{\rm s}$)	$\rm Dec._{mm}$ ($^\circ$:$'$:$''$)
J033244.01−274635.2$^{\star,\circ,\bullet,\heartsuit}$	UDF1	$2.698 \pm 0.002^{e,a}$	03:32:44.04	−27:46:36.01	03:32:44.04	−27:46:36.01	–	–
J033238.53−274634.6$^{\star,\circ,\bullet,\heartsuit}$	UDF3	2.543 ± 0.005^{e}	03:32:38.55	−27:46:34.57	03:32:38.55	−27:46:34.57	–	–
J033236.94−274726.8*	UDF5	1.759 ± 0.008^{b}	03:32:36.96	−27:47:27.13	03:32:36.97	−27:47:27.28	–	–
J033239.74−274611.4*	UDF8	1.549 ± 0.005^{e}	03:32:39.74	−27:46:11.64	03:32:39.73	−27:46:11.24	–	–
J033240.73−274749.4*	UDF10	2.086 ± 0.006^{b}	03:32:40.75	−27:47:49.09	03:32:40.73	−27:47:49.27	–	–
J033240.06−274755.5*	UDF11	$1.9962 \pm 0.0014^{c,d}$	03:32:40.07	−27:47:55.82	03:32:40.06	−27:47:55.28	–	–
J033235.07−274647.6*	UDF13	2.497 ± 0.008^{b}	03:32:35.09	−27:46:47.78	03:32:35.08	−27:46:47.57	–	–
J033243.19−275514.3$^{\triangle,\heartsuit}$	ALESS067.1	$2.1212^{+0.0014}_{-0.0005}{}^{e,j}$	03:32:43.20	−27:55:14.16	03:32:43.3	−27:55:17	03:32:43.18	−27:55:14.49
J033246.83−275120.9$^{\spadesuit,\circ}$	AzTEC.GS25	2.292 ± 0.001^{g}	03:32:46.83	−27:51:20.97	03:32:46.96	−27:51:22.4	03:32:46.84	−27:51:21.23
J033247.59−274452.3$^{\diamond,\circ,\heartsuit}$	AzTEC.GS21	1.910 ± 0.001^{h}	03:32:47.59	−27:44:52.43	03:32:47.60	−27:44:49.3	03:32:47.59	−27:44:52.32
J033212.55−274306.1$^{\heartsuit}$	AzTEC.GS22	1.794 ± 0.005^{i}	03:32:12.52	−27:43:06.00	03:32:12.60	−27:42:57.9	03:32:12.56	−27:43:05.37

Notes. Identification codes (ID) in the first two columns refer to (∗) GOODS (IAU); (∗∗) (sub-)millimetre surveys available in the literature (Yun et al. 2012; Hodge et al. 2013; Targett et al. 2013; Dunlop et al. 2017). Spectroscopic redshifts and ALMA, *HST*, and LABOCA-AzTEC (labelled as mm) sky positions are listed in the central columns. References for ALMA counterparts: ($^\triangle$) Hodge et al. (2013); ($^\spadesuit$) Fujimoto et al. (2017); (*) Dunlop et al. (2017); ($^\diamond$) Hatsukade et al. (2018); ($^\circ$) Cowie et al. (2018); ($^\bullet$) Franco et al. (2018); ($^\heartsuit$) Pantoni et al., in preparation). References for spectroscopic redshifts (uncertainty at least on the third decimal digit): (a) Szokoly et al. (2004) found $z_{\rm H\,\alpha} = 2.688 \pm 0.005$, consistent with Pantoni et al., in preparation measurement within 2σ; (b) Momcheva et al. (2016); (c) Kurk et al. (2013); (d) Dunlop et al. (2017); (e) Pantoni et al., in preparation; (f) Straughn et al. (2009); (g) Popesso et al. (2009); (h) Vanzella et al. (2008); (i) Targett et al. (2013) and reference therein; (j) Kriek et al. (2006, 2007) found $z_{\rm H\,\alpha} = 2.122 \pm 0.053$, consistent with Pantoni et al., in preparation measurement within the uncertainties.

the optical domain ($\lambda_{\rm obs} = 0.3$–1 μm); six or more detections in the NIR+MIR bands ($\lambda_{\rm obs} = 1$–25 μm); two or more detections in the FIR band ($\lambda_{\rm obs} = 25$–400 μm); spectroscopically confirmed redshift in the range $1.5 < z < 3$; and one or more detections and/or upper limits in the radio and X-ray regimes.

In more details, we selected our sample from the catalogues by Yun et al. (2012), Targett et al. (2013), and Dunlop et al. (2017), which are built on (sub-)millimetre surveys of the GOODS-S field that used either ALMA ($\lambda_{\rm B6} = 1.1$–1.4 mm, covering $\sim$1 arcsec^2 in the HUDF South), LABOCA ($\lambda = 0.870$ mm) on APEX or AzTEC ($\lambda = 1.1$ mm) on ASTE (now on LMT). Then, we exploited the wide and deep broad-band coverage of GOODS-S field to associate the (sub-)millimetre sources with the UV/optical and Infrared photometry currently available in literature and radio and X-ray public catalogues. In particular, we used data from the MUltiwavelength Southern Infrared Catalogue[2] (GOODS-MUSIC; Grazian et al. 2006b), whose UV/optical/NIR photometry was associated with *Spitzer* and *Herschel* infrared photometry by Magnelli et al. (2013); the $\simeq$7-Ms *Chandra* Deep Field South Catalogue (Luo et al. 2017b), for the emission in the X-ray; and the VLA radio catalogues by Miller et al. (2013b), Thomson et al. (2014), and Rujopakarn et al. (2016).

Herschel photometry is crucial to sample the dust FIR peak of $z \sim 2$ galaxies and to constrain the dust thermal emission and the intrinsic (i.e. unobscured) stellar light. For these reasons, we included in our study only sources that are detected at least in two *Herschel* (either PACS or SPIRE) photometric bands. Thus, we associated the NIR-selected sources of GOODS-MUSIC catalogue with the *Herschel*-detected source in the catalogue by Magnelli et al. (2013). As a result, we obtained a UV–optical–IR photometric catalogue made of 263 sources, which we matched with the aforementioned (sub-)millimetre catalogues as we describe in the following. We associated the millimetre sources observed in the ALMA survey by Dunlop et al. (2017) using a searching radius of 1 arcsec, compatible with ALMA and *HST* beam size; the (sub-)millimetre sources by Yun et al. (2012) and Targett et al. (2013) surveys using a 1.5-arcsec searching radius from the optical CANDELS coordinates and a 3-arcsec radius from the NIR IRAC ones (both consistent with the respective beam size). From these two matches, we obtained 29 secure associations, 11 in Dunlop et al. (2017) and 18 in Yun et al. (2012) and Targett et al. (2013) catalogues. Due to our selection criteria, these sources are faint, but not completely obscured, in the UV/optical rest-frame band (sampled by ACS/*HST* and WFC3/*HST*, with a magnitude limit $m_{\rm AB,\,lim} = 25$–26 mag; Windhorst & Cohen 2010), bright in the IR rest-frame domain (sampled by SPIRE/*Herschel*, with a 5σ confusion limited fluxes of ~ 24.0, 27.5, and 30.5 mJy at $\lambda = 250$, 350, and 500 μm, respectively; Nguyen et al. 2010; Oliver et al. 2012), and detected in the FIR rest frame with the following flux limits: 1.2 mJy beam^{-1} at $\lambda = 0.87$ μm (5σ, including confusion noise; LABOCA); 0.48–0.73 mJy beam^{-1} at $\lambda = 1.1$ mm (5σ, including confusion noise; AzTEC); and 35 μJy at $\lambda = 1.3$ mm (rms; ALMA).

To fulfill our selection criterion on source redshift, we used the ESO compilation of GOODS/CDF-S spectroscopy,[3] the millimetre spectroscopy by Tacconi et al. (2018), the millimetre catalogues cited above and references therein, and we selected, between the resulting 29 sources, only the ones with spectroscopic redshift in the range $1.5 < z_{\rm spec} < 3$. The latter is a stringent condition in order to properly constrain the physical properties of galaxies by fitting their SED. In particular, we choose all the sources having a measurement of their redshift from optical/millimetre spectral lines with a precision on the third decimal place (at least). The resulting 11 sources are listed in Table 1: the first 7 have an ALMA counterpart, and the last 4 an AzTEC-LABOCA. Hence, we built a multiwavelength sample composed by 11 (sub-)millimetre selected DSFGs, with a robust spectroscopic measurement of their redshift ($z_{\rm spec} \sim 2$).

To complete the multiband information, we looked for their X-ray counterparts in the $\simeq$7-Ms *Chandra* Deep Field South Catalogue by

[2]GOODS-MUSIC is a multiband catalogue ($\lambda = 0.3$–8.0 μm) of NIR (i.e. Z and $K_{\rm s}$) selected objects in the GOODS-S field. It includes two images in the U filter by ESO; one image in the B band by the VIMOS/VLT; the ACS/*HST* images in B, V, i, z bands; the ISAAC-VLT photometry (J, H, $K_{\rm s}$ bands); and the IRAC/*Spitzer* photometry at $\lambda = 3.5,\ 4.5,\ 5.8,\ 8$ μm.

[3]*Spectroscopy Master Catalogue*, publicly available at the web page https://www.eso.org/sci/activities/garching/projects/goods.html (updated to 2012).

Table 2. Up-to-date available UV–optical, infrared, (sub-)millimetre, radio and X-ray photometry, and other spectral information (CO transition) for our sample.

ID	B^a	V^a	i^a	z^a	J^b	H^b	K_s^b	$IR_{36}{}^c$	$IR_{45}{}^c$	$IR_{58}{}^c$	$IR_{80}{}^c$	$IRS_{16}{}^c$	$F_{24}{}^c$	$F_{70}{}^d$	$F_{100}{}^d$	$F_{160}{}^d$
UDF1	✓	✓	✓	✓	✓	✓	✓	✓	✓	✓	✓	nd	✓	nd	✓	✓
UDF3	✓	✓	✓	✓	✓	✓	✓	✓	✓	✓	✓	✓	✓	nd	✓	✓
UDF5	✓	✓	✓	✓	✓	✓	✓	✓	✓	✓	✓	✓	✓	nd	✓	✓
UDF8	nd	✓	✓	✓	✓	✓	✓	✓	✓	✓	✓	✓	✓	nd	✓	✓
UDF10	✓	✓	✓	✓	✓	✓	✓	✓	✓	✓	✓	nd	nd	nd	✓	✓
UDF11	✓	✓	✓	✓	✓	✓	✓	✓	✓	✓	✓	✓	✓	nd	✓	✓
UDF13	✓	✓	✓	✓	✓	✓	✓	✓	✓	✓	✓	nd	✓	nd	✓	nd
ALESS067.1	✓	✓	✓	✓	✓	✓	✓	✓	✓	✓	✓	nd	✓	nd	✓	✓
AzTEC.GS25	✓	✓	✓	✓	✓	nd	✓	✓	✓	✓	✓	nd	✓	nd	✓	✓
AzTEC.GS21	✓	✓	✓	✓	✓	nd	✓	✓	✓	✓	✓	✓	✓	✓	✓	✓
AzTEC.GS22	nd	✓	✓	✓	✓	✓	✓	✓	✓	✓	✓	nd	✓	nd	nd	✓

$F_{250}{}^e$	$F_{350}{}^e$	B9^g	$F_{500}{}^e$	$F_{870}{}^f$	B7^g	$F_{1100}{}^h$	B6^g	B4^g	B3^g	C band^i	L band^i	610 MHz^j	X-ray^k	CO line
✓	✓		✓		✓		✓			✓			✓	J(3–2)
nd	nd		nd		✓		✓			✓			✓	J(3–2)
✓	✓		nd				✓			✓			nd	
✓	✓		nd				✓			✓			✓	J(2–1)
nd	nd		nd				✓			nd			✓	
✓	✓		nd				✓			✓			✓	
nd	✓		nd				✓			✓			✓	
✓	✓		✓	✓	✓	nd		✓	✓		✓	✓	✓	J(3-2)
✓	✓		✓		✓	✓					✓		✓	
✓	✓	✓	nd		✓	(✓)	✓				✓		✓	
✓	✓	✓	nd			✓					✓		nd	

Notes. UV–optical and NIR photometry from MUSIC catalogue (Grazian et al. 2006b): (*a*) ACS-*HST*, $\lambda_c = 0.433$, 0.594, 0.771, 0.886 μm; (b) ISAAC-VLT, $\lambda_c = 1.255$, 1.656, 2.163 μm; (c) *Spitzer*, $\lambda_c = 3.6$, 4.5, 5.8, 8, 16, 24 μm. FIR photometry from Magnelli et al. (2011b, 2013), as result from the sky-match between GOODS-MUSIC catalogue and MIPS-*Herschel* photometry: (d) PACS-*Herschel*, $\lambda_c = 70$, 100, 160 μm; (e) SPIRE-*Herschel*, $\lambda_c = 250$, 350, 500 μm. Millimetre and radio photometry from Miller et al. (2013b), Yun et al. (2012), Hodge et al. (2013), Targett et al. (2013), Thomson et al. (2014), Dunlop et al. (2017), Rujopakarn et al. (2016), Fujimoto et al. (2017), Hatsukade et al. (2018), Franco et al. (2018), and Cowie et al. (2018), resulting from the cross-match with GOODS-MUSIC catalogue: (f) LABOCA/APEX, $\lambda_c = 870$ μm; (g) ALMA, $\lambda_c = 0.450$, 0.870–1, 1.3, 2, 3mm; (h) AzTEC/ASTE, $\lambda_c = 1100$ μm; (i) JVLA, $\nu_c = 6$, 1.49 GHz; (j) GMRT, $\nu = 610$ MHz. X-ray data resulting from the catalogue by Luo et al. (2017b): (k) *Chandra* ACIS, 0.5–7.0 keV. CO spectral lines by Pantoni et al. (in preparation). Checkmark stands for *detection*; nd stands for *non-detection/upper limits*; void means the source has not been observed with the corresponding device. Brackets mean that the source is detected but the data have not be taken in consideration.

Luo et al. (2017b).[4] We performed a sky match using a search radius of 1.5 arcsec. For 9 sources out of the 11 in our sample, we found a robust association (separation $\lesssim$0.7 arcsec). No association has been found for the remaining two sources, neither in the main or in the ancillary low significance catalogues.

In the radio regime, the seven (sub-)millimetre sources by Dunlop et al. (2017) have been followed up at 6 GHz by Rujopakarn et al. (2016) and just six are detected. Yun et al. (2012), Targett et al. (2013), and Thomson et al. (2014) identified their AzTEC-LABOCA sources in the 1.4-GHz VLA deep map of GOODS-S field by Miller et al. (2013b). From this association, all the four AzTEC-LABOCA sources in our sample (ALESS067.1, AzTEC.GS25, AzTEC.GS21, AzTEC.GS22) own a robust radio counterpart. Moreover, ALESS067.1 has an additional detection at 610 MHz by the Giant Metre-Wave Radio Telescope (GMRT; Thomson et al. 2014). As to UDF10, the (sub-)millimetre source without a secure radio detection (i.e. radio flux $<3\sigma$), we take into consideration just the upper limits reported in the aforementioned reference articles.

For completeness, we searched for other ALMA counterparts in the recent catalogues by Hodge et al. (2013) at $\lambda = 870$ μm (ALMA B7); Fujimoto et al. (2017), the so-called DANCING ALMA catalogue at $\lambda_{B7}/\lambda_{B6} = 0.8$–$1.1/1.1$–$1.4$ mm; Hatsukade et al. (2018) at $\lambda_{B6} = 1.1$–1.4 mm; Franco et al. (2018) in the ALMA Band 6 and centred at $\lambda = 1.13$ mm; and Cowie et al. (2018) in the ALMA Band 7, centred at $\lambda = 850$ μm. Three objects selected from LABOCA-AzTEC surveys show robust associations within 1 arcsec (ALESS067.1, AzTEC.GS25, AzTEC.GS21; see Table 1), as well as two objects selected from the ALMA survey by Dunlop et al. (2017), i.e. UDF1 and UDF3 (see Table 1). Due to blending, we discarded the AzTEC data for AzTEC.GS21, corresponding to two ALMA detections, and we considered only the ALMA counterpart associated with the IRAC source (i.e. ASAGAO.ID6; see Hatsukade et al. 2018, their section 3.4). Finally, we complemented the millimetre continuum with public ALMA data from the ALMA Science Archive[5] that will be presented in Pantoni et al. (in preparation), along with the CO line detections that we found for four objects of the sample (UDF1, UDF3, UDF8, ALESS067.1). In Table 2, we provide a schematic summary of the currently available photometry (and CO molecule spectroscopy) for each source of the sample, which

[4]They mapped the CDF-S ($\sim$500 arcmin^2, centred in the GOODS-S field) in the 0.5–7 keV band with an on-axis exposure time of $\simeq$7 Ms, reaching a sensitivity of $\simeq 1.9 \times 10^{-17}$ erg s^{-1} cm^{-2}. Images in the sub-bands at 0.5–2 and 2–7 keV have been then produced and they reach a sensitivity of $\simeq 6.4 \times 10^{-18}$ and $\simeq 2.7 \times 10^{-17}$ erg s^{-1} cm^{-2}, respectively.

[5]https://almascience.eso.org/asax/.

will be used to perform the SED fitting (Section 3) and exploited for the subsequent analysis (Sections 4 and 5).

We note that most of the studies on high-z DSFGs conduced in the last couple of years by exploiting SED fitting (e.g. da Cunha et al. 2015; Casey et al. 2017; Donevski et al. 2020; Franco et al. 2020; Dudzevičiūtė et al. 2021) focus on, e.g. galaxy location with respect the star-forming main sequence (i.e. the empirical relation between stellar mass and SFR followed by star-forming galaxies; see Daddi et al. 2007; Noeske et al. 2007); the search of diagnostic quantities, such as the dust-to-stellar mass ratio, in order to disentangle high-z main-sequence and starburst galaxies and probing the evolutionary phase of massive objects; the evolution of SFR, stellar mass, stellar attenuation, and dust mass with redshift; the difference between populations of DSFGs selected in the FIR or in the (sub-)millimetre domain; the link between star formation surface density and gas depletion time; and their role in determining the galaxy subsequent evolution.

In this work, on the one hand, we reduce the uncertainties on the constrained parameters by both selecting solely the sources with spectroscopically confirmed redshift at the peak of Cosmic SFH and requiring an accurately sampled SED from the X-ray to radio regime, with particular care on the FIR peak and the optical/NIR emission by stars, which are essential to constrain interstellar dust attenuation, galaxy age and SFR. Moreover, when combined together, these requirements allow to get an insight on both the role of DSFGs in the cosmic stellar mass assembly and galaxy co-evolution with central SMBH.

On the other hand, the requirement for a complete multiband coverage and the condition on the availability of spectroscopic redshift do not allowed us to include in our sample objects that are totally obscured in the UV/optical, and seriously limit our sample size and completeness. Even if we are not able to trace statistical indications, it is enough to test our approach to extract information on the sources, as we will describe in the following sections.

3 SED FITTING WITH CIGALE

We use the Code Investigating GAlaxy Emission (CIGALE; Boquien et al. 2019) to model the SEDs of our 11 high-z DSFGs. CIGALE is a PYTHON code that can reproduce galaxy broad-band emission – from FUV to radio wavelengths – by physically preserving an energy balance between stellar light emitted in optical/UV and re-radiated in IR. To this aim, a large grid of models is fitted to the data. In a nutshell, CIGALE builds composite stellar populations by combining single stellar population with flexible SFHs, calculates the ionized gas emission from young stars, and exploits flexible attenuation curves to attenuate both the stellar and the ionized gas emission. Infrared emission is estimated by balancing the energy absorbed from the optical/UV domain and the energy re-emitted at longer wavelengths by dust. The main physical properties, such as SFR, attenuation, dust luminosity, stellar mass, AGN fraction, are estimated by means of χ^2 and Bayesian analysis. In this section, we briefly describe the modules we have exploited to model galaxy SEDs and explain which are the main motivations that have driven our choices. In Table 3, we provide the complete list of the modules we used and the priors we assumed for the corresponding free parameters.

3.1 Star formation history

One of the more influential but yet scarcely constrained components of SED fitting is the functional form of galaxy star formation history (SFH). Since a large variation in the SFH can yield similar SEDs, broad-band fitting alone can not really provide certain information on the past star formation phases of galaxies. This problem led to the exploitation of quite simple SFHs, such as constant, exponential (decaying or rising), delayed, or periodic (e.g. Elbaz et al. 2018); in the case of high-z DSFGs, additional bursts of star formation are often included (e.g. Ciesla, Elbaz & Fensch 2017; Forrest et al. 2018; Donevski et al. 2020).

In this work, we assume a delayed exponential SFH, basing our choice on many studies of SED modelling for high-z star-forming galaxies (e.g. Papovich et al. 2011; Smit et al. 2012; Moustakas et al. 2013; Steinhardt et al. 2014; Cassarà et al. 2016; Citro et al. 2016), which suggest a slow power-law increase of galaxy SFR over a time-scale $\tau_\star$ (i.e. burst duration), followed by a rapid exponential decline. In particular, for $\tau \lesssim \tau_\star$, we adopt the functional form used by Mancuso et al. (2016b):

$$\mathrm{SFR}(\tau) \propto \left(\frac{\tau}{\tau_\star}\right)^{0.5} \qquad \text{for} \quad \tau \lesssim \tau_\star \tag{1}$$

(see their equation 3 and Fig. 3, top panel, dashed line). We simplify the evolution for $\tau > \tau_\star$ by assuming that star formation stops at $\tau \sim \tau_\star$, quenched by AGN feedback. The latter assumption is validated by the observed fraction of far-IR-detected host galaxies in the X-ray (e.g. Mullaney et al. 2012; Page et al. 2012; Rosario et al. 2012) and optically selected AGNs (e.g. Mor et al. 2012; Wang et al. 2013; Willott, Bergeron & Omont 2015), indicating that SFR in massive ($M_\star > 10^{10}$ M$_\odot$) galaxies is abruptly stopped by AGN feedback, after $\tau_\star$, over a very short time-scale, i.e. $<10^7$–10^8 yr. As such, the adopted SFH has just one free parameter, i.e. the main star-forming burst duration ($\tau_\star$). We assume $\tau_\star$ to vary in the range [0.15–2] Gyr (see Table 3), as it is suggested by recent observations with ALMA, characterizing the dust-enshrouded star formation of massive high-redshift galaxies (e.g. Scoville et al. 2014, 2016), and by the observed α-enhancement, i.e. iron underabundance compared to α elements, in local ellipticals (see the review by Renzini 2006).

3.2 Stellar component

We compute the stellar light following the prescriptions in Bruzual & Charlot (2003). We divide the stellar population into two simple stellar populations (SSPs): young stars, which are supposed to be completely enshrouded into their molecular birth clouds (BCs), and old stars, which live in the ISM and have already dissolved their BCs. We set the separation age between these two components as a free parameter, fixing the priors (see Table 3) to the typical values found to be valid for star-forming progenitors of massive ellipticals (e.g. Schurer et al. 2009). We assume a Chabrier (2003) initial mass function (IMF; $M_\star = 0.1$–100 M$_\odot$) and we set the stellar metallicity to the solar one, i.e. $Z = 0.02$.

3.3 Stellar light attenuation by dust

In order to model interstellar dust attenuation in the UV/optical, we adopt a double power-law (Lo Faro et al. 2017, see their equations 5 and 6), reproducing the different contributions from young and old stars.

We prescribe the light from young stars to be completely absorbed by dust in the surrounding BC by fixing the BC attenuation in the V band to the value $A_\mathrm{V}^\mathrm{BC} = 10^4$. The energy balance provided by CIGALE ensures that the light absorbed by dust is re-emitted in the FIR (i.e. dust thermal emission). To be self-consistent, we fix the slope δ_BC to the dust FIR spectral index (β_dust) best value, as it is obtained by the fitting procedure.

Table 3. Input parameters configuration used to fit the broad-band emission of our $z \sim 2$ DSFGs with CIGALE.

CIGALE module	Shape	Free parameters	Symbol	Values
Star formation history	Constant[a]	Age (Gyr)	$\tau_\star$	2, 1.5, 1.0, 0.8, 0.7, 0.6, 0.5, 0.4, 0.3, 0.2, 0.15
Single stellar population	Two SSPs[b]	Initial mass function	IMF	Chabrier (fixed)
		Metallicity	Z	0.02 (fixed)
		Separation age (Myr)	$\Delta_\star$	10, 20, 30, 50, 100, 150, 200
Dust attenuation	Double power law[c]	V-band attenuation in BCs	A_V^{BC}	10000 (fixed)
		Power-law slope in BCs	δ_{BC}	$-1.6, -1.8, -2.0, -2.2, -2.4, -2.6$
		A_V^{ISM}/A_V^{BC}	f_{att}	0.0001, 0.0002, 0.0003
		Power-law slope in ISM	δ_{ISM}	$-0.7, -0.5, -0.3, -0.1$
Dust emission	Power law + Single-T modified BB[d]	MIR power-law slope	α_{dust}	1.6, 1.8, 2.0, 2.2
		Dust emissivity index	β_{dust}	1.6, 1.8, 2.0, 2.2, 2.4, 2.6
		Dust temperature (K)	T_{dust}	20, 30, 40, 50, 60, 70

Notes. Columns show (in order) the input CIGALE modules we used (CIGALE module); the functional shape assumed for the modelled quantity (when required; Shape); list of module free parameters (units in square brackets; Free parameters); free parameter symbol (Symbol); and prior values for the corresponding parameter (Values). References for the adopted shapes are (a) Mancuso et al. (2016b), (b) Bruzual & Charlot (2003), (c) Lo Faro et al. (2017), and (d) Casey (2012).

After $t_0 \sim 10^7$ yr from their birth, old stars have already dissipated/escaped their BC, and the light they emit is expected to be attenuated just by dust populating galaxy ISM (whose V-band attenuation is defined by the relation $f_{att} = A_V^{ISM}/A_V^{BC}$). Following the prescriptions in Lo Faro et al. (2017), we allow the ISM attenuation slope δ_{ISM} to span the range: $[-0.7, -0.5, -0.3, -0.1]$ (see Table 3).

We refer the reader to Appendix A for the detailed derivation of individual galaxy attenuation law (see Fig. 1, right-hand column).

3.4 Dust emission

We model the IR interstellar dust emission by decomposing the IR light into two different components: a power law, describing the mid-IR (MIR) emission coming from polycyclic aromatic hydrocarbon (PAHs) and central AGN; a single-temperature modified blackbody (BB), describing the far-IR (FIR) thermal emission of cold interstellar dust, as suggested by Casey (2012). This simple approach is very convenient in our case since the MIR SED of our 11 DSFGs is scarcely sampled (each source owns just one or two photometric data points in this spectral range). We exploit the fitting formula shown in Casey (2012, her equation 3), providing a more accurate fit to those systems with fewer MIR photometric data. The function has three free parameters: the MIR power-law slope α_{dust}, the dust emissivity index β_{dust}, and the dust temperature T_{dust}.

We set the spectral index α_{dust} to vary in the range [1.6, 1.8, 2.0, 2.2], following the results obtained by Mullaney et al. (2011). The value of β_{dust} is usually assumed to be 1.5 and historically ranges between 1 and 2 (see e.g. Hildebrand 1983). Some recent works suggest a wider range for β_{dust}, between 1 and 2.5 (e.g. Casey et al. 2011; Chapin et al. 2011; Bianchi 2013; Gilli et al. 2014; Bianchini et al. 2019; Pozzi et al. 2020), favouring the higher values in the range (i.e. $\beta_{dust} > 1.5$). For this reason, we set the dust spectral index β_{dust} to freely vary in the range [1.6–2.6]. The dust temperature T_{dust} can vary between 20 and 70 K, which almost corresponds to the normal range of dust temperatures expected for galaxy ISM heated only by star formation (see Table 3). A more realistic approach is the one assuming more than one family of cold dust grains (i.e. with different temperatures) populating the galaxy ISM. However, fitting the dust thermal emission with a multitemperature modified BB requires at least more than five photometric data points in the FIR regime, which are currently not available for every source of the sample.

We avoid to model the AGN MIR emission alone since the most quoted AGN models (e.g. Fritz, Franceschini & Hatziminaoglou 2006; Nenkova et al. 2008; Feltre et al. 2012) are extremely complex and characterized by a number of free parameters that would be hardly constrained by the undersampled MIR emission of our galaxies. In addition, considering the absence of any spectral information in the MIR band, we fairly avoid the exploitation of more sophisticated models that include PAH and silicate lines, such as Draine & Li (2007). We would like to stress that these choices do not affect significantly the derived value of the IR total luminosity. Indeed, the net effect of the MIR emission coming from both AGN and PAHs on the integrated IR luminosity attains less than 10–20 per cent, meaning that the cold-dust modified BB still dominates the bulk of the total IR emission, when integrated. This fact has been recently demonstrated by the analysis of a (local) sample of IR galaxies hosting a moderate powerful X-ray AGN (i.e. $L_{2-10\,keV} \sim 10^{42}$–$10^{44}$ erg s^{-1}) by Mullaney et al. (2011), and it is still valid for our 11 DSFGs (as we discuss in Section 4.4).

Finally, it is important to take into consideration that the method we use is *luminosity-weighted*: Dust temperature is estimated from the modified BB FIR peak, which is more sensitive to the warmest population of dust grains. As such, the single-temperature SED fitting procedure tends to return values of T_{dust} higher than the mean one. This tendency and how it affects the SED-derived dust mass have been widely discussed and investigated in the last decade, both in local and high-z Universe (e.g. Dale et al. 2012; Magdis et al. 2012; Berta et al. 2016; Schreiber et al. 2018; Liang et al. 2019; Martis et al. 2019). Magdis et al. (2012) quantify this effect on a statistical sample of $z \gtrsim 2$ sub-millimetre galaxies (SMGs), finding that the fit with single-temperature modified BB gives dust masses that are (on average) lower by a factor of $\sim$2 when compared with Draine & Li (2007) model. We will extensively comment on this result in Sections 4.2 and 4.3, where we discuss the derivation of dust and gas masses for our sample.

4 RESULTS

In this Section we present and comment the information extracted from galaxy multiwavelength emission. In Fig. 1 (left-hand column) we show the best SEDs (thick solid black lines) for the 11 (sub-)millimetre selected star-forming galaxies of our sample, as obtained by the broad-band SED fitting performed with CIGALE. The con-

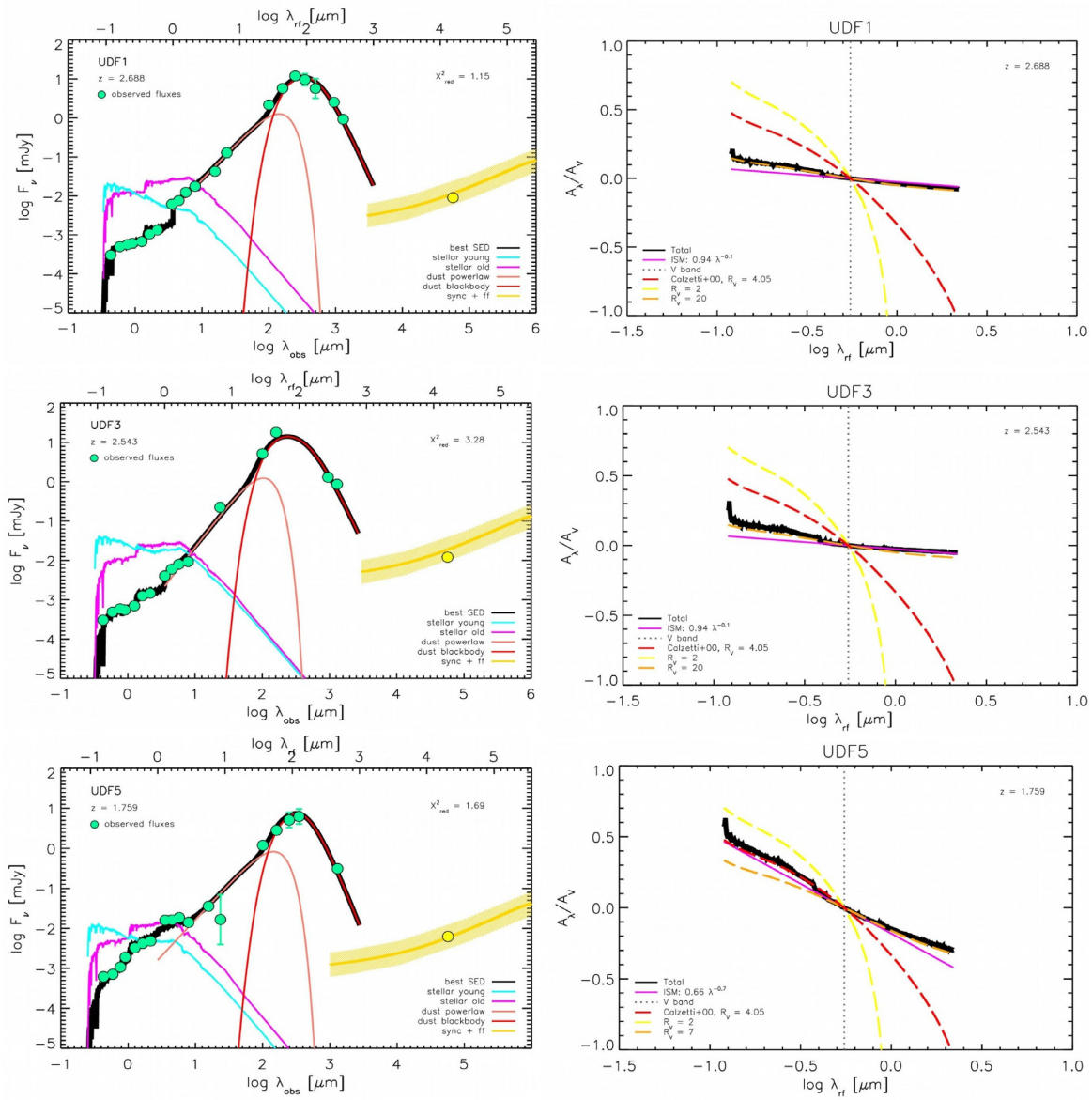

Figure 1. Galaxy best SEDs (left-hand column) and best attenuation laws (right-hand column). Left-hand panels: Thick solid black line stands for the total best galaxy SED; solid cyan line indicates the UV/optical/NIR emission coming from young stars; solid magenta line stands for the old stars UV/optical/NIR emission; solid orange line represents the warm dust MID power law; solid red line shows the cold dust FIR modified BB emission; thick solid yellow line represents the radio emission coming solely from host galaxy star formation; green filled circles are the observed fluxes included in SED fitting; and yellow filled circles are the observed fluxes in the radio bands (not included in the fit). Error bars are omitted for clarity when they are comparable to the symbol size. Right-hand panels: Thick solid black line stands for the total best attenuation law; solid magenta line is the ISM attenuation law; dashed red line represents the standard Calzetti attenuation law; and dashed yellow and orange lines are the Calzetti attenuation laws obtained by decreasing (yellow) or increasing (orange) the standard value for R_V, as it is indicated in the legends.

tribution of each component to the total SED is colour-coded and comprises of the UV/optical/NIR emission coming from young stars (i.e. enshrouded in their BC; see Section 3.2); the UV/optical/NIR emission of old stars (i.e. in the galaxy ISM, outside their BC; see Section 3.2); and the warm dust MID power law and the cold dust FIR modified BB (Casey 2012, see Section 3.4). The spectroscopic redshift of each source and the reduced χ^2 (i.e. $\chi^2_{\rm red} = \chi^2/{\rm dof}$) are written on the corresponding panel. For reference, we add the predicted radio emission coming solely from the host galaxy star formation (solid yellow line; its derivation will be described in Section 4.5). The observed fluxes in the radio band (at $\nu_{\rm obs}$ = 6 GHz, 1.4 GHz, 610 MHz; yellow filled circles) are consistent with the yellow solid line (within the uncertainties). We do not include radio photometry in SED fitting since we want to avoid any strong assumption on the radio-to-(sub)mm spectral index. The latter is well constrained when at least two fluxes in the radio band are available, but this requirement is satisfied only for one source, i.e. ALESS067.1.

The main physical quantities characterizing our galaxies (e.g. SFR, $\tau_\star$, $M_{\rm star}$, $T_{\rm dust}$) are obtained both with χ^2 analysis and Bayesian analysis. The latter approach estimates galaxy physical properties from likelihood-weighted parameters on a fixed grid of models (whose set up for this work has been described in the previous Sections), exploring the parameter space around the given priors

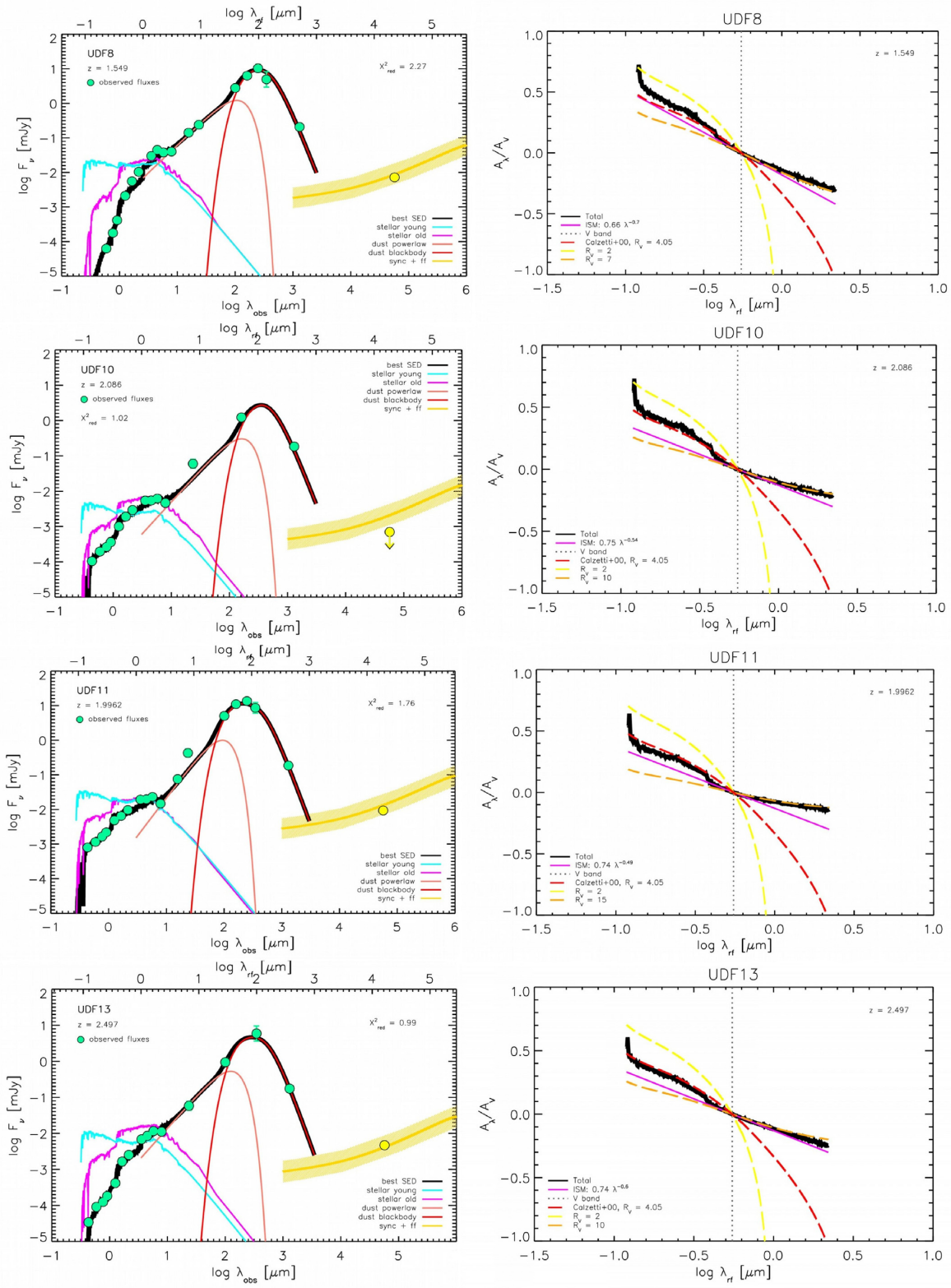

Figure 1 – *continued*

(listed in Table 3). We expect this analysis to provide the most precise and accurate estimations of the main SED-inferred quantities and we list the corresponding outcomes in Tables 4 and 5, along with their uncertainties. We note that these quantities are well constrained only if the probability distribution function (pdf) is well behaved (e.g. single peak). This is the case for the majority of the marginalized pdfs. The most common exceptions are found for: the BC-to-ISM V-band attenuation, $f_{\rm att}$; the BC attenuation spectral index, $\delta^{\rm BC}$; and

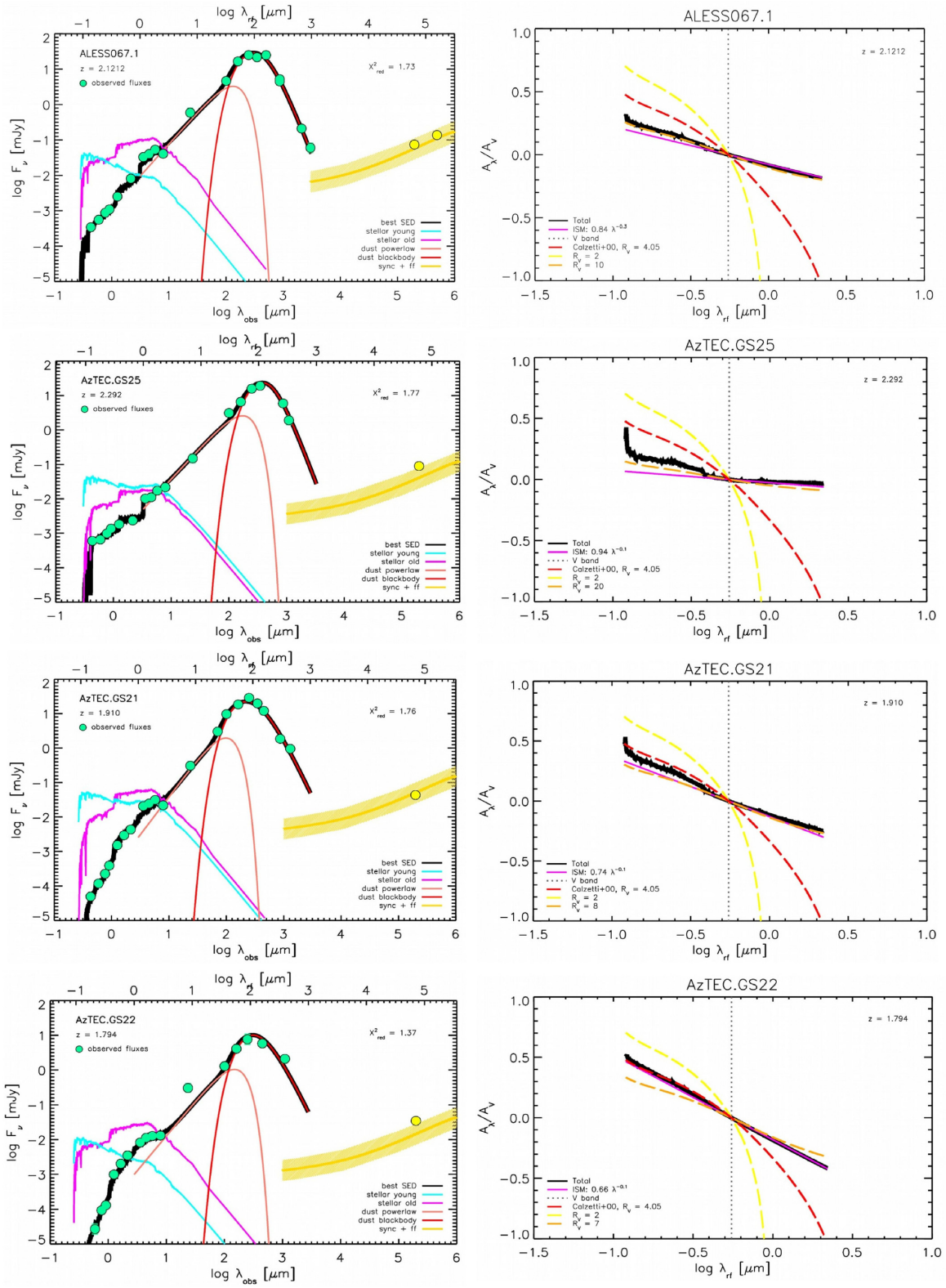

Figure 1 – *continued*

the separation age between the old and young SSPs, $\Delta_\star$. Finally, the χ^2 analysis has been exploited to have a hint on fits goodness, i.e. $\chi^2_{\rm red} \sim 1$ (cf. Table 4, second column).

Given the outcomes listed in Tables 4 and 5, in the following we discuss the resulting attenuation laws for our objects (Section 4.1), we derive their dust and gas masses (Sections 4.2 and 4.3) and provide the analysis on their X-ray and radio emission (Sections 4.4 and 4.5). Finally, we collect from literature the multiwavelength sizes of our objects and convert them to the corresponding circularized radii (Section 4.6).

Table 4. CIGALE outputs from stellar (star formation + emission + attenuation) Bayesian analysis for the sources of the sample (ID and spectroscopic redshift in the first two columns).

ID	$z_{\rm spec}$	χ^2_{red}	SFR ($M_\odot$ yr^{-1})	$\tau_\star$ (Myr)	$M_\star$ (10^{10} $M_\odot$)	$\Delta_\star$ (Myr)	$M_{\rm R}$ (10^{10} $M_\odot$)	$f_{\rm att}$ (10^{-4})	$\delta^{\rm BC}$	$\delta^{\rm ISM}$
UDF1	2.698	1.15	352 ± 18	334 ± 58	8 ± 1	10.0 ± 0.5	3.3 ± 0.6	3.0 ± 0.2	−2.1 ± 0.3	−0.1 ± 0.003
UDF3	2.543	3.28	519 ± 38	234 ± 47	9 ± 1	30 ± 4	3.2 ± 0.6	3.0 ± 0.2	−2.1 ± 0.3	−0.1 ± 0.002
UDF5	1.759	1.69	85 ± 6	404 ± 85	2.4 ± 0.3	20 ± 1	1.0 ± 0.2	1.0 ± 0.05	−2.1 ± 0.3	−0.7 ± 0.003
UDF8	1.549	2.27	100 ± 5	992 ± 50	6.5 ± 0.3	160 ± 23	3.4 ± 0.2	2.0 ± 0.1	−2.4 ± 0.3	−0.7 ± 0.003
UDF10	2.086	1.02	41 ± 5	917 ± 137	2.5 ± 0.3	50 ± 9	1.2 ± 0.2	1.0 ± 0.05	−2.1 ± 0.3	−0.54 ± 0.08
UDF11	1.9962	1.76	241 ± 19	380 ± 82	6.4 ± 0.9	51 ± 9	2.6 ± 0.5	1.0 ± 0.05	−2.1 ± 0.3	−0.49 ± 0.09
UDF13	2.497	0.99	111 ± 17	879 ± 149	6.5 ± 1.4	51 ± 58	3.3 ± 0.8	1.8 ± 0.4	−2.1 ± 0.3	−0.6 ± 0.1
ALESS067.1	2.1212	1.73	487 ± 24	903 ± 100	29 ± 3	10.0 ± 0.6	15 ± 2	3.0 ± 0.2	−1.8 ± 0.3	−0.3 ± 0.003
AzTEC.GS25	2.292	1.77	401 ± 20	290 ± 88	8 ± 2	29 ± 20	3 ± 1	2.5 ± 0.5	−2.1 ± 0.3	−0.1 ± 0.008
AzTEC.GS21	1.910	1.76	360 ± 18	746 ± 105	18 ± 2	50 ± 3	9 ± 1	3.0 ± 0.5	−2.0 ± 0.3	−0.5 ± 0.004
AzTEC.GS22	1.794	1.37	91 ± 5	940 ± 74	5.7 ± 0.5	11 ± 4	2.9 ± 0.3	3.0 ± 0.5	−2.4 ± 0.3	−0.7 ± 0.01

Notes. The third column shows the corresponding best-fitting reduced χ^2. In the order, we list the outcomes from: SFH module (SFR and galaxy age $\tau_\star$, i.e. the burst duration), stellar emission (stellar mass, $M_\star$; age separation between old and young stars, $\Delta_\star$; restituted gas mass to ISM from stellar evolution, $M_{\rm R}$) and stellar attenuation (ISM-to-BC V-band attenuation, $f_{\rm att}$; BC attenuation spectral index, $\delta^{\rm BC}$; ISM attenuation spectral index, $\delta^{\rm ISM}$). Units are indicated between square brackets.

Table 5. CIGALE outputs from dust emission Bayesian analysis for the sources of the sample (ID in the first column).

ID	$\alpha_{\rm dust}$	$\beta_{\rm dust}$	$T_{\rm dust}$ (K)	$L_{\rm dust}$ (10^{12} $L_\odot$)
UDF1	1.80 ± 0.09	2.0 ± 0.3	56 ± 3	3.5 ± 0.2
UDF3	2.2 ± 0.1	2.1 ± 0.3	73 ± 4	4.9 ± 0.3
UDF5	1.80 ± 0.09	2.3 ± 0.3	42 ± 3	0.77 ± 0.04
UDF8	1.60 ± 0.08	2.2 ± 0.3	52 ± 4	1.10 ± 0.06
UDF10	1.9 ± 0.1	2.1 ± 0.3	46 ± 7	0.41 ± 0.05
UDF11	2.2 ± 0.1	2.5 ± 0.2	69 ± 4	2.2 ± 0.2
UDF13	1.8 ± 0.1	2.3 ± 0.3	60 ± 3	1.2 ± 0.2
ALESS067.1	1.80 ± 0.09	2.2 ± 0.2	50 ± 3	5.4 ± 0.3
AzTEC.GS25	1.80 ± 0.09	2.3 ± 0.2	40 ± 2	3.9 ± 0.2
AzTEC.GS21	2.2 ± 0.1	1.8 ± 0.2	63 ± 3	3.9 ± 0.2
AzTEC.GS22	1.9 ± 0.1	1.8 ± 0.3	40 ± 2	1.01 ± 0.06

Note. In the order, we list MIR power-law spectral index ($\alpha_{\rm dust}$), FIR modified-BB spectral index ($\beta_{\rm dust}$), dust temperature ($T_{\rm dust}$), and dust luminosity ($L_{\rm dust}$) in units of 10^{12} $L_\odot$.

4.1 Attenuation law

In Fig. 1, we show the attenuation law (i.e. $A_\lambda/A_{\rm V}$; thick solid black line) obtained as described in Appendix A by adopting the prescriptions already explained in Section 3.3.

We note that the overall emerging stellar emission is mostly shaped by dust attenuation in the ISM ($\sim\lambda^{-\delta^{\rm ISM}}$, with $0.1 \leq \delta^{\rm ISM} \leq 0.7$; solid magenta line). Indeed, we modelled dust extinction in BCs to absorb almost all the radiation from young stars enshrouded in these dense environments. Some emission from young stars emerges just at $\lambda_{\rm rest} \gtrsim 10$ μm, where dust extinction is less effective.

Focusing on the total (i.e. ISM + BC) attenuation law ($A_\lambda/A_{\rm V}$), we note two main different behaviours in λ. For the majority of our galaxies (7 out of 11 sources), the attenuation law is well described by a standard Calzetti et al. (2000, i.e. $R_{\rm V} = A_{\rm V}/E(B-V) \simeq 4.05 \pm 0.80$; dashed red line) at wavelengths bluer than $\lambda_{\rm V} = 540$ nm, while it shows a flattening towards redder wavelengths, with a characteristic $R_{\rm V}$ ranging between 7 and 15 (cf. with dashed orange and yellow line). The other five objects show a flatter attenuation law at every λ, with an $R_{\rm V} \simeq 20$. This flattening of the attenuation law towards high-z (Calzetti law is constrained in local star-forming galaxies like Milky Way) may be caused by a more uniformly mixed geometry of the interstellar dust grains or it may simply indicate diverse dust grains geometries and distributions into the ISM, which are very difficult to be constrained at $z > 1$ (e.g. Salmon et al. 2016; Leja et al. 2017; Narayanan et al. 2018; Salim, Boquien & Lee 2018; Buat et al. 2019; Trayford & Schaye 2019). Because of the smaller amount of reddening at near-infrared wavelengths, the standard Calzetti has been found to significantly lower SFR and stellar mass when applied to high-z dusty galaxies (e.g. Williams et al. 2019). Exploiting such a locally calibrated attenuation law at high-z should be done with caution, in particular while dealing with the UV/optical-to-millimetre emission of DSFGs.

4.2 Dust mass

We derive the dust mass for each source, given a measure of dust flux in the rest-frame Rayleigh–Jeans (R-J) regime and the Bayesian estimation of dust temperature. It is well known (e.g. Bianchi 2013; Gilli et al. 2014; D'Amato et al. 2020; Pozzi et al. 2020) that dust mass can be estimated in the optically thin approximation ($\tau_\nu \ll 1$) as

$$M_{\rm dust} = \frac{S(\nu_{\rm obs})\, d_{\rm L}^2}{(1+z)\, k(\nu_{\rm rest})\, B_{\rm BB}(\nu_{\rm rest}, T_{\rm dust})}, \quad (2)$$

where $S(\nu_{\rm obs})$ is the observed flux such as $\nu_{\rm rest} = \nu_{\rm obs}(1+z)$ is in the R-J regime; $B_{\rm BB}$ is the BB brightness computed at $\nu_{\rm rest}$, with $T_{\rm dust}$ being the dust equilibrium temperature derived by performing the single-T fit of the FIR SED; $k(\nu_{\rm rest}) = 5.1\,(\nu_{\rm rest}/1.2\,{\rm THz})^\beta$ cm^2 g^{-1} is the dust absorption coefficient per unit of mass (e.g. Magdis et al. 2012; Gilli et al. 2014); $d_{\rm L}^2$ is the luminosity distance; and $(1+z)$ takes into account the k-correction entering in the relation between flux and luminosity.

In order to obtain the most reliable estimate of dust mass, we exploited the reddest (sub-)millimetre observed flux for each source. In Table 6, we list the corresponding rest-frame wavelength, which lies to a good extent in the R-J regime. We estimated errors on dust mass following error propagation theory. However, dust masses derived from single-temperature fit to the FIR SED are *luminosity-weighted*. As a consequence, we select a dust temperature that is typically slightly higher than the mean and the resulting dust mass tends to be underestimated. Magdis et al. (2012) attempted to quantify

Table 6. For each source of the sample (ID in column 1), we list of the values for the quantities entering in equation (2) (values for $\beta_{\rm dust}$ and $T_{\rm dust}$ can be found in Table 5) and the resulting dust mass ($M_{\rm dust}$; last column, in units of 10^8 $M_\odot$).

ID	$d_{\rm L}$ (Mpc)	$\lambda^{\rm rest}_{\rm dust}$ (μm)	$\nu^{\rm rest}_{\rm dust}$ (GHz)	$S_{\rm dust}$ (mJy)	$M_{\rm dust}$ (10^8 $M_\odot$)
UDF1	22 886.4	353	850	0.924 ± 0.076^a	2.8 ± 1.0
UDF3	21 294.4	367	817	0.863 ± 0.084^a	2.0 ± 0.8
UDF5	13 553.1	471	637	0.311 ± 0.049^a	2.3 ± 1.1
UDF8	11 588.6	510	588	0.208 ± 0.046^a	1.21 ± 0.67
UDF10	16 711.9	421	712	0.184 ± 0.046^a	0.95 ± 0.67
UDF11	15 833.4	434	691	0.186 ± 0.046^a	0.73 ± 0.33
UDF13	20 825.4	372	806	0.174 ± 0.045^a	0.60 ± 0.34
ALESS067.1	17 058.3	279	1075	4.5 ± 0.4^b	4.8 ± 1.8
AzTEC.GS25	18 755.5	334	898	1.9 ± 0.6^c	6.8 ± 4.1
AzTEC.GS21	14 997.8	445	674	0.954 ± 0.074^a	2.9 ± 0.7
AzTEC.GS22	13 885.7	394	761	2.1 ± 0.6^c	7 ± 4

Notes. In particular, $\nu^{\rm rest}_{\rm dust}$ ($\equiv \lambda^{\rm rest}_{\rm dust}$>200 μm) is the rest-frame frequency corresponding to the observed R-J flux $S_{\rm dust} \equiv S(\nu_{\rm obs})$. Units are reported between square brackets. Dust masses are not corrected by Magdis et al. (2012): A factor of 2 must be added. [a]ALMA flux at $\lambda_{\rm obs} = 1300$ µm ($\nu_{\rm obs} = 230$ GHz). [b]ALMA flux at $\lambda_{\rm obs} = 870$ µm ($\nu_{\rm obs} = 345$ GHz). [c]AzTEC flux at $\lambda_{\rm obs} = 1100$ µm ($\nu_{\rm obs} = 273$ GHz).

Table 7. CO analysis: $L_{\rm CO}$ and $M_{\rm H_2}$ for UDF1, UDF3 UDF8, and ALESS067.1 by Pantoni et al. (in preparation), assuming an $\alpha_{\rm CO} = 3.6$ K km pc^2 s^{-1} $M_\odot^{-1}$.

ID	$z_{\rm CO}$	CO line	$L_{\rm CO}$ (10^8 K km s^{-1} pc^2)	$M_{\rm H_2}$ (10^{10} $M_\odot$)
UDF1	2.698	J(3–2)	31 ± 3	2.6 ± 0.7
UDF3	2.543	J(3–2)	170 ± 10	15 ± 3
UDF8	1.5490	J(2–1)	122 ± 9	5.8 ± 1.1
ALESS067.1	2.1212	J(3–2)	196 ± 31	16.8 ± 5.4

this effect, which turns out to shift downwards dust masses of a factor of ∼2 (cf. Sections 3.4 and 4.3).

4.3 Gas mass

CIGALE does not allow to derive galaxy gas mass directly from broad-band fitting: gas masses computed by the stellar emission module consist solely of the gas fraction that is restituted to the medium by stellar evolution (i.e. $M_{\rm R}$; see Table 4). We derive the gas masses for our 11 DSFGs by relying either on CO line luminosities (when available) or on R-J interstellar dust continuum.

Although CO lines require to assume a conversion factor $\alpha_{\rm CO}$ (to convert the observed CO line luminosity into the galaxy molecular hydrogen mass, H_2) and an excitation ladder (in case of transitions with $J > 1$), they provide the most direct method to infer the molecular gas content in high-z DSFGs.

In Table 7, we list the CO-derived H_2 masses for four sources of our sample (UDF1, UDF3, UDF8, ALESS067.1) by Pantoni et al. (in preparation), who use the same approach, tool, and prescriptions adopted in this work. We note that the H_2 mass, when multiplied by a factor of 1.36 that accounts for helium, provides the total molecular gas mass of the galaxy with a very good approximation. We derive the molecular hydrogen mass from $J > 1$ CO line luminosities, converted to the equivalent CO(1–0) luminosity following Daddi et al. (2010), Daddi et al. (2015), by assuming the same excitation ladder, i.e. $r_{31} = 0.42 \pm 0.07$ and $r_{21} = 0.76 \pm 0.09$, and CO conversion factor, i.e. $\alpha_{\rm CO} = 3.6$ $M_\odot$(K km s^{-1} pc^2)$^{-1}$. Although the topic is still under debate, a smaller value of $\alpha_{\rm CO} \sim 0.8$–1 (often exploited for local ULIRGs and high-z compact DSFGs) is commonly thought to be inappropriate for the globally distributed molecular gas and more advisable for high-resolution observations that isolate the nuclear region (e.g. Scoville et al. 2016; Carilli & Walter 2013, for a review).

Observing CO lines at high-z is very expensive in terms of time-on-source ($\gtrsim$ a few hours) and so they are available just for a small number of DSFGs. Alternative methods are mainly based on the exploitation of continuum far-IR thermal emission coming from cold interstellar dust but they are affected by larger uncertainties since they need to assume a gas-to-dust ratio (GDR). Nevertheless, they are very convenient for high-z massive dusty galaxies: Indeed their dust continuum can be detected, e.g. by ALMA, in just a few minutes of observing time. The two most popular methods exploiting dust R-J continuum are developed and described in the articles by Leroy et al. (2011) and Scoville et al. (2014, 2016), to which we refer for the following analysis. We note that these two approaches have been recently combined in the work by Liu et al. (2019) on the A3 COSMOS[6] sample.

We derived the total gas mass, i.e. H I + H_2, using the local relation by Leroy et al. (2011, their section 5.2):

$$\log_{10}({\rm GDR}) = \log_{10}\frac{M_{\rm H\,I} + M_{\rm H_2}}{M_{\rm dust}} = (9.4 \pm 1.1) - (0.85 \pm 0.13)[12 + \log_{10}({\rm O/H})]. \quad (3)$$

The dependence on gas metallicity allows to extend the result to $z \lesssim 3$. We derived the gas metallicity for our $z \sim 2$ sample of DSFGs using the mass–metallicity relation by Genzel et al. (2012, their section 2.2), following Elbaz et al. (2018, their section 2.4):

$$12 + \log_{10}({\rm O/H}) = -4.51 + 2.18 M_\star - 0.0896\,(\log_{10} M_\star)^2. \quad (4)$$

The rms dispersion of mass–metallicity relation at $z \sim 2$ is of about 0.09 dex. Systematic uncertainties between different metallicity indicators and calibrators can reach ∼0.3 dex (e.g. Kewley & Ellison 2008) and clearly dominate over the statistical one. The outcomes are shown in Fig. 6. In order to derive the total gas mass (equation 3), we used our SED-inferred dust masses (cf. Table 6) corrected following Magdis et al. (2012). As discussed in Section 4.2, this procedure brings into the total dust mass budget also the coldest interstellar dust, whose content is (on average) a factor of ∼2 underestimated when a single-temperature modified BB is used to fit the FIR interstellar dust thermal emission. The resulting total gas masses $M_{\rm gas,\,tot}$ are listed in Table 8. The uncertainty is of about 0.3 dex. We note that metallicities could be even higher, in case of very compact FIR sources ($r_{\rm FIR} < 1$ kpc) and possibly dust thick. Actually, the inferred total gas masses strongly depend on the method and, in our case, on the assumed mass–metallicity relation, shown in equation (4).

We estimated the molecular ISM masses of our 11 DSFGs using the empirical calibration by Scoville et al. (2016, cf. their fig. 1, right-hand panel):

$$\frac{L_{\nu_{850\,\mu{\rm m}}}}{M_{\rm gas,mol}} = 6.2 \times 10^{19} \left(\frac{L_{\nu_{850\,\mu{\rm m}}}}{10^{31}}\right)^{0.07}. \quad (5)$$

The resulting molecular gas masses $M_{\rm gas,\,mol}$ are listed in Table 8. The corresponding uncertainty is of about 0.3 dex. We note that our

[6]https://sites.google.com/view/a3cosmos.

Table 8. Molecular gas mass $M_{\rm gas,\,mol}$ derived following the approach in Scoville et al. (2016); total (H I+H_2) gas mass $M_{\rm gas,\,tot}$ and gas metallicity $Z_{\rm gas}$ evaluated following Genzel et al. (2012) and Elbaz et al. (2018).

ID	$\log M_{\rm gas,\,mol}$ ($M_\odot$)	$\log M_{\rm gas,\,tot}$ ($M_\odot$)	GDR	$Z_{\rm gas}$ 12+log(O/H)
UDF1	10.5	10.8	120	8.61
UDF3	10.6	10.7	119	8.62
UDF5	10.1	10.9	161	8.46
UDF8	10.0	10.5	126	8.59
UDF10	9.8	10.5	159	8.47
UDF11	9.8	10.3	127	8.58
UDF13	9.7	10.2	127	8.59
ALESS067.1	10.9	11.0	100	8.71
AzTEC.GS25	10.6	11.2	121	8.61
AzTEC.GS21	10.7	10.8	106	8.68
AzTEC.GS22	10.7	11.3	130	8.57

Notes. Uncertainties have been omitted for clarity: They are ∼0.3 dex for molecular gas masses and ∼0.4 dex for total gas masses and gas metallicities.

two estimates for gas mass (i.e. $M_{\rm gas,\,mol}$ and $M_{\rm gas,\,tot}$) are compatible within the errors.

4.4 X-ray emission

The X-ray emission from a star-forming galaxy can be traced back to two main different processes: the star formation itself, since massive, compact binaries can produce X-ray radiation (the so-called *X-ray binaries*), and the accretion of matter on to the central SMBH (if the AGN is *on*), since the infalling heated material radiate (also) in the X-ray band. Thus, the X-ray luminosity of a star-forming galaxy can provide a wealth of information on the possible presence of a central AGN and on its evolutionary stage.

As described in Section 2, 9 sources of our sample out of 11 own a robust counterpart in the recent and very deep X-ray *Chandra* catalogue by Luo et al. (2017b), based on an ≈ 7-Ms map of the CDF-S. We note that the two X-ray non-detections (UDF5 and AzTEC.GS22) lie in very deep regions of the *Chandra* map (equivalent exposure times are ∼6.22 and ∼5.80 Ms, respectively), thus the hypothesis of totally obscured X-ray sources is the most probable.

For every X-ray source, Luo et al. (2017b) provide the 0.5–7.0 keV *intrinsic* luminosity, i.e. net of the Milky Way and X-ray source intrinsic absorption, the latter determined by the intrinsic column density $N_{\rm H,int}$. In Appendix B, we calculate the corresponding 2–10 keV luminosity, in order to easily compare with literature while investigating galaxy-BH co-evolution. Intrinsic 2–10 keV luminosities ($L_{\rm X}$) for our nine sources with an X-ray counterpart are listed in Table 9.

4.4.1 X-ray dominant component

Luo et al. (2017b) provide also a classification of the X-ray sources (i.e. AGN, galaxy or star), which we show for reference in Table 9 (column 12 – classX – Luo et al.).They classified as *X-ray AGN* every X-ray source that shows at least one indication on the presence of a central AGN emitting in the X-rays (for a detailed description of the criteria they used we refer the reader to their Section 4.5 and references therein). However, it does not imply that the AGN X-ray emission prevails over the galactic one.

To get a deeper insight on this topic, in Fig. 2, we compare the 2–10 keV luminosity of our sources with their infrared luminosity (derived from SED fitting; see Table 5). We note every source falling above the relation by Ranalli, Comastri & Setti (2003) for star-forming galaxies to be an AGN, meaning that its X-ray luminosity overwhelms the one coming from the host galaxy. In Fig. 2, these sources are marked with a blue circle. This result is still valid when the evolution of X-ray binaries luminosity with galaxy redshift, SFR, and $M_\star$ is taken into consideration (e.g. Lehmer et al. 2016). Note that the two *AGN-dominated* X-ray sources are also in the 3-Ms XMM catalogue by Ranalli et al. (2013).

Actually, many recent works have shown that the X-ray luminosity from the central AGN (if present) begins to be comparable to the host galaxy one at $L_{\rm X} \approx 10^{42}$ erg s^{-1} (e.g. Bonzini et al. 2013; Padovani et al. 2015). Indeed, this value is commonly adopted to clearly discern the nuclear X-ray emission from that associated to star formation $L_{\rm X,\,SFR} \approx 7 \times 10^{41}$ erg s^{-1} SFR/10^2 $M_\odot$ yr^{-1} (e.g. Vattakunnel et al. 2012). In Fig. 2, we represent this threshold with a dashed black line. We note that almost all the sources with an X-ray counterpart lie above it, possibly indicating that a X-ray quasar is growing in the nuclear region of the host galaxy. We refer the reader to Section 5 for a further analysis on this topic.

4.4.2 AGN fraction in the IR domain

In the following, we exploit the 2–10 keV luminosity $L_{\rm X}$ to infer the fraction of IR luminosity (i.e. integrated over 8–1000 μm) coming from the central AGN, in a way that is totally independent from SED fitting and avoids all the caveats related to parameter degeneracies (see Section 3.4). In particular, we exploit the correlation by Mullaney et al. (2011, their equation 4),

$$\log\left(\frac{L_{\rm IR}^{\rm AGN}}{10^{43}\ {\rm erg\ s^{-1}}}\right) = (0.53 \pm 0.26) + (1.11 \pm 0.07)\ \log\left(\frac{L_{\rm X}}{10^{43}\ {\rm erg\ s^{-1}}}\right), \quad (6)$$

to derive the AGN infrared luminosities and the corresponding AGN fraction (i.e. $f_{\rm AGN}^{(1)} = L_{\rm IR}^{\rm AGN}/L_{\rm IR}^{\rm dust}$), which we list in Table 10. Infrared luminosities (Table 10) come from the SED fit with CIGALE, following the approach by Casey (2012, Section 3.4).

The correlation by Mullaney et al. (2011) is based on a sample of 25 local (i.e. z <0.1) AGNs from the *Swift*-BAT survey, with typical X-ray and IR properties (i.e. $N_{\rm H}$, $L_{2-10\,{\rm keV}}$, and $L_{\rm IR}$) largely covering the same ranges as those $z \sim 2$ AGNs and star-forming galaxies detected in *Chandra* (e.g. CDF-N and CDF-S; see fig. 1 in Mullaney et al. 2011) and *Spitzer*/*Herschel* deep surveys (e.g. GOODS; see Section 2). Thus, we can reasonably apply the result from Mullaney et al. (2011) to our sample of $z \sim 2$ DSFGs. It follows that the central AGN contribution to the total infrared light of our X-ray detected DSFGs is negligible (i.e. consistent with 0 or a few per cent): it attains values ≲10 per cent once the 1σ scatter (i.e. ∼0.5 dex) of Mullaney et al. correlation is considered. A similar result has been found by Pozzi et al. (2012) analysing a sample of ∼30 *Herschel*-selected $z \sim 2$ LIRGs: Just the ∼35 per cent of the sample show the presence of an AGN at the 3σ confidence level, but its contribution to the IR emission accounts for only ∼5 per cent of the energy budget.

We provide a further investigation on the AGN fraction by referring to the relation between the nuclear 12-μm luminosity ($L_{12\,\mu{\rm m}}^{\rm nuc}$) and the intrinsic 2–10 keV luminosity by Asmus et al. (2015, their equation 1) found for a local sample but valid also at higher redshift (see also Gandhi et al. 2009). We exploited the 2–10 keV luminosities $L_{\rm X}$ (Table 10) to derive the expected rest-frame 12-μm nuclear luminosity of our sources. Comparing the outcome with the

Table 9. In this table, we list IDs of the source associations (ID: this work; ID_X: G102) and their angular separation (d) in arcsec; source redshifts (z); 2–10 keV intrinsic luminosities at redshift z (L_X); the class (AGN or galaxy) associated with each source by Luo et al. (2017b) and the X-ray dominant component (active nucleus or host galaxy) found by our analysis.

ID	ID_X	d (arcsec)	z	L_X (10^{42} erg s^{-1})	Class X Luo et al.	X dominant component
UDF1	805	0.69	2.698	40.2	AGN	AGN
UDF3	718	0.54	2.544	1.8	AGN	galaxy
UDF8	748	0.07	1.549	36.3	AGN	AGN
UDF10	756	0.31	2.086	0.6	galaxy	galaxy
UDF11	751	0.29	1.996	1.7	galaxy	galaxy
UDF13	655	0.26	2.497	2.1	AGN	galaxy
ALESS067.1	794	0.40	2.1212	3.8	AGN	galaxy
AzTEC.GS25	844	0.71	2.292	6.1	AGN	galaxy
AzTEC.GS21	852	0.36	1.91	1.7	AGN	galaxy

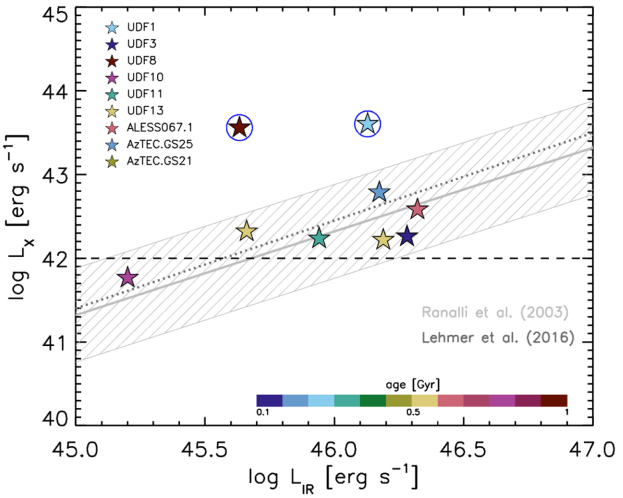

Figure 2. X-ray luminosity versus IR luminosity. Stars stand for the sources with an X-ray counterpart in the catalogue by Luo et al. (2017b). They are colour-coded by age (i.e. $\tau_\star$). IR luminosities (8–1000 μm rest frame) result from SED fitting. Grey line represents the correlation between X-ray and IR luminosity when they are ascribed to star formation solely by Ranalli et al. (2003), with its 1σ scatter. Dark grey dotted line represents the trend followed by our objects when the evolution with galaxy z, $M_\star$, and SFR is taken into account in the relation by Lehmer et al. (2016). Its 1σ scatter (of about 0.4 dex) has not been plotted for clarity. The two outliers are highlighted with a blue circle. The dashed horizontal black line indicates the value at which X-ray luminosity from the central BH begins to be comparable to the one coming from star formation.

corresponding observed luminosity at $\lambda_{rest} = 12$ μm, we derive the fraction coming from the nucleus $f^{(2)}_{AGN}$, which we show in the last column of Table 10. The MIR-X-ray correlation scatter of 0.34 dex do not allow us to precisely constrain the AGN fraction, but still we can provide a qualitatively estimation of the impact of the central AGN on the observed MIR emission: The fraction of 12- μm luminosity coming from the nucleus attains to values $\lesssim$10 per cent and for the majority of our sources (seven out of nine) it is $\lesssim$1 per cent.

We note that the two X-ray non-detected sources (UDF5 and AzTEC.GS22) do not appear also in the supplementary catalogue at very low significance. This may indicate either that no (not very powerful) AGN is present or that it is highly obscured, i.e. *Compton-thick*, with $N_H \gtrsim 10^{24}$ cm^{-2}. However, we can not provide an insight on this issue just basing on the (other) multiwavelength data at our disposal.

Finally, we cross-checked our results with the outcomes obtained by fitting our DSFG SEDs including the modules from Draine & Li (2007) and Fritz et al. (2006) in the CIGALE routine, while keeping the free parameters fixed to the values found in literature to better reproduce the high-z DSFG emission (see e.g. Małek et al. 2018; Donevski et al. 2020). The resulting AGN fraction f_{AGN} is still smaller than 10 per cent for almost all the DSFGs of our sample. A similar result has been recently found by Barrufet et al. (2020) by analysing the IR SED of $\sim$ 200 DSFGs in the COSMOS field at 0.7 $< z_{phot} <$ 5.6. These evidences provide a further confirmation of our approach in modelling the MIR and FIR emission, as it is discussed in Section 3.4.

4.5 Radio emission

The radio emission in star-forming galaxies can be traced back to two different astrophysical processes: the star formation itself and the accretion of the central SMBH, which can eventually turn into an AGN emitting in the radio band (cf. Mancuso et al. 2017).

Radio emission associated with star formation comprises two components: free–free emission coming from H II regions that contain massive, ionizing stars, fully dominating at frequencies $\nu >$ 30 GHz; synchrotron emission resulting from relativistic electrons accelerated by supernova remnants. In the following, we consider both these contributions to provide a rough but realistic estimate of the stellar radio emission for each galaxy of the sample by using the SFR from our SED fitting (see Section 3). We adopt the classical free–free emission calibration with SFR at 33 GHz for a pure hydrogen plasma ($Z_i = 1$) with temperature $T = 10^4$ K by Murphy et al. (2012):

$$L_{ff} \approx 3.75 \times 10^{26} \mathrm{erg\,s^{-1}\,Hz^{-1}} \frac{\mathrm{SFR}}{\mathrm{M_\odot\,yr^{-1}}} \left(\frac{T}{10^4\,\mathrm{K}}\right)^{0.3} \times g(\nu,\ T)\ \exp\left(-\frac{h\nu}{kT}\right), \quad (7)$$

where $g(\nu,\ T)$ is the Gaunt factor: approximated according to Draine (2011). Synchrotron calibration with SFR is a bit controversial since it involves complex and poorly understood processes, such as the production and escaping rates of relativistic electrons and the magnetic field strength. Here we exploit the calibration proposed by Murphy et al. (2011, 2012), but see also the review by Kennicutt & Evans (2012). Thus, the synchrotron luminosity ascribed to star

Table 10. In this table, we list IDs of the sources; 2–10 keV luminosities (L_X); total infrared luminosities (8–1000 μm rest frame) obtained from SED fitting (L_{IR}^{dust}, as described in Section 3.4); infrared AGN luminosities and AGN fractions ($f_{AGN}^{(1)}$) inferred following Mullaney et al. (2011; equation 6); and AGN fraction inferred by using Asmus et al. (2015) MIR-X-ray correlation ($f_{AGN}^{(2)}$).

ID	L_X (10^{43} erg s^{-1})	L_{IR}^{dust} (10^{43} erg s^{-1})	L_{IR}^{AGN} (10^{43} erg s^{-1})	$f_{AGN}^{(1)}$ (per cent)	$f_{AGN}^{(2)}$ (per cent)
UDF1	4.0 ± 0.4	1345 ± 67	16 ± 13	1	6
UDF3	0.18 ± 0.02	1910 ± 114	0.5 ± 0.3	0.03	0.2
UDF8	3.6 ± 0.4	430 ± 21	14 ± 11	3	14
UDF10	0.060 ± 0.006	159 ± 19	0.15 ± 0.07	0.09	1
UDF11	0.17 ± 0.02	873 ± 59	0.5 ± 0.3	0.06	0.5
UDF13	0.21 ± 0.02	458 ± 75	0.6 ± 0.4	0.1	0.8
ALESS067.1	0.38 ± 0.04	2096 ± 105	1.2 ± 0.7	0.06	0.4
AzTEC.GS25	0.61 ± 0.06	1493 ± 75	2 ± 1	0.1	1
AzTEC.GS21	0.17 ± 0.2	1546 ± 77	0.5 ± 0.3	0.03	0.3

Table 11. In this table, we list in the order IDs of the sources; the observed frequency in the radio band (ν^{obs}); the corresponding radio fluxes from free–free (F_{ff}) and synchrotron emission (F_{sync}) by using equations (7) and (8), for which we adopted a scatter of 0.3 dex; and the observed radio flux (F_{radio}^{obs}) and their uncertainties.

ID	ν^{obs} [GHz]	F_{ff} [μJy]	F_{sync} [μJy]	F_{radio}^{obs} [μJy]
UDF1	5.25	4.0	7.6	9.0 ± 0.6
UDF3	5.25	4.5	0.6	12.1 ± 0.6
UDF5	5.25	2.0	3.8	6.3 ± 0.5
UDF8	5.25	3.0	5.7	7.2 ± 0.5
UDF10	5.25	0.7	1.4	<0.7
UDF11	5.25	4.6	8.7	9.3 ± 0.7
UDF13	5.25	1.4	2.7	4.7 ± 0.5
ALESS067.1	1.5	9.4	47.3	74 ± 7
	0.61	10.1	100.3	137 ± 15
AzTEC.GS25	1.5	6.8	34.1	90 ± 6
AzTEC.GS21	1.5	8.4	42	44 ± 6
AzTEC.GS22	1.5	2.4	12.1	35 ± 7

Note. Units are given in square brackets.

formation can be written as follows:

$$L_{sync} \approx 1.9 \times 10^{28} \mathrm{erg\,s^{-1}\,Hz^{-1}} \frac{SFR}{M_\odot\,yr^{-1}} \left(\frac{\nu}{GHz}\right)^{-\alpha_{sync}} \times \left(1 + \left(\frac{\nu}{20\,GHz}\right)^{0.5}\right)^{-1} \times \frac{1 - \exp(-\tau_{sync}(\nu))}{\tau_{sync}(\nu)}, \quad (8)$$

where $\alpha_{sync} \sim 0.75$ is the spectral index found for high-z DSFGs (e.g. Condon 1992; Ibar et al. 2009, 2010; Thomson et al. 2014), the term $(1 + \nu^{0.5})^{-1}$ renders spectral aging effects (see Banday & Wolfendale 1991), and the latter factor takes into account synchrotron self-absorption in terms of the plasma optical depth (e.g. Kellermann 1966; Tingay & de Kool 2003).

Then, we compare these predictions with the observed radio fluxes (Table 11) in order to get some hints on the presence (or not) of a central AGN. For every source we find the radio emission to be consistent with galaxy star formation (see Fig. 1): Radio fluxes lie within the scatter of free–free plus synchrotron radio emission, represented by the yellow shaded area. It is worth noticing, though, which this evidence does not exclude the presence of a central AGN, whose radio emission could be simply too low to emerge from the stellar one. We pinpoint three possible scenarios: the galaxy does not host an AGN; the galaxy host an accreting central SMBH but it does not contribute to the observed emission in the radio band; an AGN is present but it is radio-silent or radio-quiet. In this respect, we provide a further analysis in Section 5.

4.6 Multiwavelength source sizes

Comparing multiwavelength sizes and centroid positions is crucial to infer the evolutionary phase of high-z DSFGs (e.g. Lapi et al. 2018) and differences in ISM conditions (e.g. Elbaz et al. 2018; Donevski et al. 2020). To homogenize the information over the whole sample, we derive the linear circularized multiwavelength radius by using the following expression:

$$r_{circ}\,[\mathrm{kpc}] = R\,[\mathrm{arcsec}]\ \sqrt{q}\ c\,[\mathrm{kpc\,arcsec^{-1}}], \quad (9)$$

when the corresponding source angular size R (i.e. half-light semi-major axis $R_{1/2}$ or effective radius R_e, the latter in case of a Sérsic profile fit of the source light profile) is available in the literature. In equation (9), q is the projected axial ratio and c is the angular-to-linear conversion factor, which depends on redshift and cosmology (see Table 12). The *HST H*-band circularized radii are derived from the angular sizes measured by van der Wel et al. (2012), who performed a Sérsic fit of the resolved sources in the CANDELS *HST* survey. The ALMA and VLA circularized radii of the HUDF sources (UDF1–UDF13) are derived from the corresponding angular sizes measured in the source deconvolved FWHM images by Rujopakarn et al. (2016), who performed a two-dimensional (2D) elliptical Gaussian fitting allowing for multiple components. This is the case of UDF11 radio counterpart (see Table 12) showing two main Gaussian components: The first is centred on the ALMA source while the second extends around it (cf. fig 1b in Rujopakarn et al. 2016). As to the AzTEC and LABOCA sources (ALESS067.1–AzTEC.GS22), (sub-)millimetre and radio sizes are not available since they are non-resolved in the corresponding maps. Just for two sources (ALESS067.1, AzTEC.GS22), we found the angular size (i.e. Sérsic effective radius R_e) of their ALMA counterparts in the DANCING ALMA catalogue by Fujimoto et al. (2017), which we exploited to derive the circularized radii.

5 DISCUSSION

In this section, we discuss our results from two diverse perspectives. First, we provide a general overview on the sample, characterizing our galaxies by exploiting the main results from SED fitting and

Table 12. Circularized radii for the multiwavelength counterparts of our (sub-)millimetre sources (when resolved in the corresponding map).

ID	c (kpc arcsec^{-1})	n_{HST}	r_{HST} (kpc)	$r_{\rm ALMA}$ (kpc)	$r_{\rm VLA}$ (kpc)
UDF1	8.121	7.2 ± 0.4	0.57 ± 0.02	1.46 ± 0.06	2.8 ± 0.1
UDF3	8.224	0.81 ± 0.02✦	1.59 ± 0.01	1.85 ± 0.06	1.48 ± 0.03
UDF5	8.632	0.71 ± 0.01	2.29 ± 0.01	1.8 ± 0.1	2.4 ± 0.1
UDF8	8.647	3.0 ± 0.02	5.68 ± 0.01	4.3 ± 0.5	2.1 ± 0.1
UDF10	8.508	1.23 ± 0.02	1.96 ± 0.01	–	–
UDF11	8.551	1.41 ± 0.01	4.50 ± 0.01	4.3 ± 0.6	3.4 ± 0.3
		–		–	0.65 ± 0.04
UDF13	8.256	1.86 ± 0.03	1.17 ± 0.01	2.6 ± 0.4	2.1 ± 0.2
ALESS067.1	8.489	7.9 ± 0.7	6.5 ± 0.2	1.0 ± 0.1	–
AzTEC.GS25	8.390	3.5 ± 0.5	1.8 ± 0.1	0.9 ± 0.04	–
AzTEC.GS21	8.586	1.50 ± 0.06	3.66 ± 0.05	–	–
AzTEC.GS22	8.624	0.22 ± 0.03✦	3.2 ± 0.1	–	–

Notes. c (third column) is the number of proper kpc at the redshift of the source; *H*-band circularized radii ($r_{\rm H}$) in the fourth column are derived from the effective Sérsic half-light semi-axis by van der Wel et al. (2012) and n is the corresponding Sérsic index of the light radial profile (fifth column); ALMA and VLA circularized radii ($r_{\rm ALMA}$ $r_{\rm VLA}$and, respectively, are listed in the last two columns. Flag ✦: The fit to the source is suspicious (van der Wel et al. 2012). Source ID in column 1.

Table 13. Median, first, and third quartiles of the following quantities (in the order): redshift (z), age of the burst ($\tau_\star$); SFR; stellar mass ($M_\star$); ISM attenuation spectral index ($\delta_{\rm ISM}$); IR luminosity ($L_{\rm IR}$); dust mass ($M_{\rm dust}$); gas mass ($M_{\rm gas}$: total and molecular); depletion time ($\tau_{\rm depl}$); AGN fraction in the IR domain ($f_{\rm AGN}$); and ALMA, *HST*, and VLA sizes ($r_{\rm ALMA}$, r_{HST}, and $r_{\rm VLA}$).

		Median	First quartile	Second quartile
z		2.086	1.794	2.497
SFR	($M_\odot$ yr^{-1})	241	91	401
$\tau_\star$	(Myr)	746	334	917
$M_\star$	(10^{10} $M_\odot$)	6.5	5.7	9
$\delta_{\rm ISM}$		−0.5	−0.1	−0.7
$f_{\rm att}$	(10^{-4})	2.5	1	3
$L_{\rm IR}$	(10^{12} $L_\odot$)	2.2	1.01	3.9
$M_{\rm dust}$	(10^8 $M_\odot$)	(2 ×)2.3	(2 ×)0.95	(2 ×)4.8
$M_{\rm gas,\,tot}$	(10^{10} $M_\odot$)	6.3	3.2	10.0
$M_{\rm gas,\,mol}$	(10^{10} $M_\odot$)	3.2	0.6	5.0
$\tau_{\rm depl}$	(Myr)	205	143	395
$f_{\rm AGN}$	(per cent)	0.8	0.4	1
$r_{\rm ALMA}$	(kpc)	1.8	1.2	3.5
r_{HST}	(kpc)	2.3	1.6	4.5
$r_{\rm VLA}$	(kpc)	2.25	2.1	2.8

Note. The (× 2) in $M_{\rm dust}$ has to be considered to apply the correction by Magdis et al. (2012) (see Section 4.2).

providing a further analysis on their multiwavelength emission, which we have extensively described in Sections 3 and 4. Then, we place the sources in the broader context of galaxy evolution, both comparing with the most popular diagnostic plots (that are empirically derived, such as galaxy main sequence; dust mass and gas mass versus stellar mass; gas metallicity relation), and predictions from theory (e.g. Pantoni et al. 2019). To this aim, we mainly refer to the *in situ* galaxy-BH co-evolution scenario (see e.g. Mancuso et al. 2016a,b, 2017; Lapi et al. 2018).

In Table 13, we list the median physical properties of the sample and the corresponding first and third quartiles. Our 11 galaxies are young (median $\tau_\star \sim 0.7$ Gyr) and forming stars at high rates, of the order of hundreds $M_\odot$ yr^{-1}, leading to stellar masses of $\sim 10^{10}$–10^{11} $M_\odot$. This very intense star formation activity is typically observed in the very central regions of the galaxies. From high-resolution imaging (when available), we found our galaxies to be compact, both in the FIR/mm (median $r_{\rm ALMA} \sim 1.8$ kpc), in the optical (median $r_{HST} \sim 2.3$ kpc), and in the radio band (median $r_{\rm VLA} \sim 2.25$ kpc). Gas-rich (median total $M_{\rm gas,\,tot} \sim 6 \times 10^{10}$ $M_\odot$; median molecular $M_{\rm gas,\,mol} \sim$ (3–4) $\times 10^{10}$ $M_\odot$) and characterized by depletion time-scales of a (few) hundred(s) of Myr (median $\tau_{\rm depl} \sim 100$ Myr), our objects are the typical high-z (sub-)millimetre star-forming galaxies whose detections have been constantly growing since the advent of ALMA (e.g. Tadaki et al. 2015; Massardi et al. 2018; Talia et al. 2018; Hodge & da Cunha 2020, for a review). They have high IR luminosities (∼ a few 10^{12} $L_\odot$), comparable to the typical values of the local ULIRGs and high-z DSFGs (see the review by Casey et al. 2014), revealing a large interstellar dust content (median $M_{\rm dust} \sim 5 \times 10^8$ $M_\odot$). AGN fraction contributing to IR emission is negligible ($f_{\rm AGN} = 1$ per cent lies in the 75th percentile). Similar values are found in literature (e.g. Elbaz et al. 2018; Barrufet et al. 2020). As to the ISM attenuation law, it results shallower (median $\delta_{\rm ISM} \sim -0.5$) than the standard Calzetti et al. (2000), constrained in local star-forming galaxies. Our results, mainly derived from the SED fitting, basically reflect the selection we have performed on the FIR/mm catalogues in the GOODS-S field to build our sample (see Section 2).

In Fig. 3, we place the galaxies of our sample on the $M_\star$–SFR plane. SFRs, stellar masses, and galaxy ages are derived from SED fitting, as described in Section 3. In the last decades, the majority of star-forming galaxies, from local to high-z Universe (at least out to $z \sim 4$), have been found to follow an empirical relation between stellar mass and SFR, the galaxy main sequence (e.g. Daddi et al. 2007; Noeske et al. 2007). In Fig. 3, we compare the position of our DSFGs with the empirical determination of galaxy main sequence by Speagle et al. (2014), at redshifts 1.7, 2, and 2.5 (colour-coded), spanning the redshift range of the sample ($z_{\rm spec} \sim 1.5$–3). We note that our sources lie in correspondence or just above the relation at the corresponding redshift.

Interpreting the diverse *loci* of star-forming galaxies on to the $M_\star$–SFR plane is very controversial, since it strongly depends on the scenario accounted for describing galaxy evolution. The debate concerning the main drivers of DSFGs formation and evolution through cosmic time is still object of intense discussions and we are currently not able to comprehensively solve the issue.To interpret our outcomes we refer to the *in situ* galaxy-BH co-evolution scenario (see

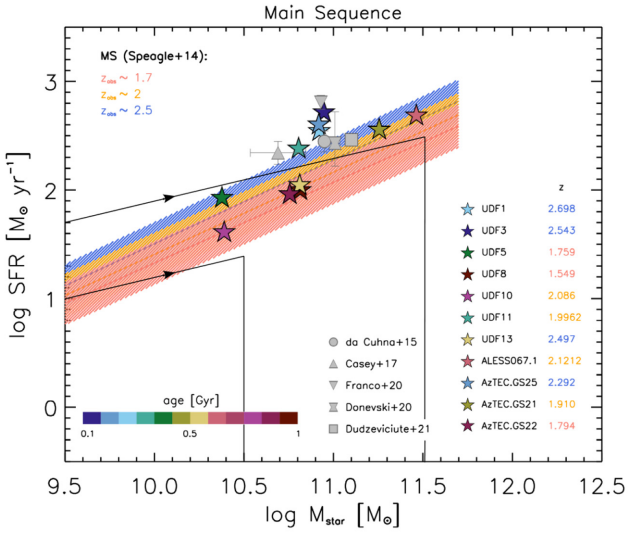

Figure 3. Empirical galaxy main sequence of star-forming galaxies by Speagle et al. (2014) at different redshifts: $z \sim 1.5$ in red, $z \sim 2$ in orange, $z \sim 3.5$ in blue, with its 1σ scatter (∼0.2 dex). Overplotted stars stand for the galaxies of this work, considering the values of SFR and $M_\star$ derived from our SED fitting. Symbols are colour-coded by galaxy age (i.e. $\tau_\star$). Error bars are compatible with symbol size. Galaxy redshift is indicated in the legend next to galaxy ID and colour-coded by the corresponding redshift bin. Grey symbols represent the median values obtained by some other existing samples of high-z DSFGs, as specified in the legend. For reference, we plot the evolutionary tracks predicted by the *in situ* co-evolution scenario (black solid lines; Mancuso et al. 2016b).

e.g. Eke, Efstathiou & Wright 2000; Fall 2002; Romanowsky & Fall 2012; Mancuso et al. 2016a,b, 2017; Shi et al. 2017; Lapi et al. 2018). Our theoretical interpretation (possibly) does not constitute the only consistent description of our results (other approaches can be found in literature, e.g. Dekel & Birnboim 2006; Hopkins et al. 2006; Calura et al. 2017; Eales et al. 2017). In the following, we want just to provide a possible and self-consistent interpretation that encompasses galaxy broad-band and spectroscopic emission, multiwavelength sizes, and galaxy co-evolution with the central SMBH. To get more details on the main steps characterizing the formation and evolution of massive high-z IR luminous galaxies, as predicted by the *in situ* scenario, we refer the reader to Lapi et al. (2018). A schematic view of galaxy typical SFH and BH accretion history (BHAH) is available in Mancuso et al. (2017, their fig. 2).

In Fig. 3, we show a pair of tracks that represent the path on to the $M_\star$–SFR plane followed by a high-z DSFG during its evolution, as predicted by the *in situ* galaxy-BH co-evolution scenario (solid black lines). Time flow is indicated by the black arrows. The starting point of galaxy evolutionary track is determined by galaxy SFR when star formation ignites. During the early phase, star formation proceeds at an almost constant rate (i.e. SFR $\propto \tau^{1/2}$ and $M_\star \propto \tau^{2/3}$, which implies SFR $\propto M_\star^{1/3}$) and, increasing its stellar mass, the galaxy approaches the main sequence of star-forming galaxies (Mancuso et al. 2016b, see their equation 7). Galaxy main sequence emerges as a statistical *locus* in the $M_\star$–SFR plane, where it is more probable to find star-forming galaxies because they spend in its vicinity most of their lifetime. Following the *in situ* scenario, the less abundant population of star-forming galaxy that has been found to lie above the main sequence (traditionally referred as *starbursts*; e.g. Rodighiero et al. 2011) is constituted by young galaxies that have still to accumulate most of their stellar mass. As soon as AGN feedback removes the fuel of star formation (effective for galaxies with $M_\star > 10^{10}$ M$_\odot$), galaxy SFR is abruptly reduced and the object moves below the main sequence, becoming a red and dead galaxy. Stars in Fig. 3 represent the objects of our sample and are colour-coded by galaxy age (i.e. $\tau_\star$), as obtained from SED fitting. Younger (i.e. bluer) objects are found to lie to the upper left-hand side of the main sequence at the corresponding redshift, while the elder (i.e. redder) are found to lie in correspondence of it, as predicted by the *in situ* scenario. All in all, these galaxies are almost main-sequence objects and we expect for them to find some signatures of obscured and/or accreting AGN, and possibly some evidences of its activity (i.e. outflows/winds). However, its contribution to the galaxy IR emission is negligible: the median value for our sample attains less than 1 per cent.

We note that the median values of stellar mass and SFR of our sample (i.e. median $M_\star \sim 6.5 \times 10^{10}$ M$_\odot$ and median SFR∼241 M$_\odot$ yr^{-1}) are consistent (i.e. lie in the same area of the $M_\star$–SFR plane) with the median values found in the most recent studies on high-z DSFGs exploiting SED fitting (e.g. da Cunha et al. 2015; Casey et al. 2017; Donevski et al. 2020; Franco et al. 2020; Dudzevičiūtė et al. 2021, grey symbols in Fig. 3) spanning the photometric redshift range $0.5 < z < 5$. These results refer to samples of different sizes, including large statistically significant samples of DSFGs selected in the FIR-millimetre domain (Donevski et al. 2020; Dudzevičiūtė et al. 2021), and smaller samples of a few tenths of objects, with different selection criteria.

The typical compactness of DSFGs revealed by ALMA in the recent past years (typical FIR radii ∼1 to a few kpc; e.g. Negrello et al. 2014; Riechers et al. 2014; Dye et al. 2015; Ikarashi et al. 2015; Simpson et al. 2015; Tadaki et al. 2015; Harrison et al. 2016; Scoville et al. 2016; Dunlop et al. 2017; Massardi et al. 2018; Talia et al. 2018), together with the evidence from high-resolution imaging that the most intense events of star formation occur in a few collapsing clumps located in this very central region of the galaxy (e.g. Hodge et al. 2019; Tadaki et al. 2019), provide an observational confirmation of the *in situ* scenario predictions for the evolution of massive high-z DSFGs. The whole multiband size evolution predicted by the *in situ* scenario (see Lapi et al. 2018) is consistent with the median optical and FIR size we found for our sample (i.e. $r_{HST} \sim 2.3$ kpc $> r_{\rm ALMA} \sim 1.8$ kpc; see Table 13) and it has been recently confirmed by Tadaki et al. (2020). Most of the sources show an optical isolated morphology, while four galaxies (UDF11, ALESS067.1, AzTEC.GS21, AzTEC.GS22; Pantoni et al., in preparation) have more complex (i.e. clumpy) morphologies, possibly indicating the presence of minor companions – that can enhance the formation of stars and prolong the star formation in the dominant galaxy by refuelling it with gas – or just being a signature of the ongoing dusty star formation. The picture is even more uncertain, since no photometric redshift has been measured for the companion candidates.

Figs 4–6 show the statistical relationships found by Pantoni et al. (2019), with their 1σ scatter, at redshifts 1.7, 2, and 2.5 (colour-coded). In this work, the authors present a new set of analytic solutions aimed at self-consistently describing the spatially averaged time evolution of the gas, dust, stellar, and metals content in star-forming galaxies, focusing on the high-z counterparts of local ETGs. The main statistical relationships are derived after setting the main parameters to follow the framework defined by the *in situ* galaxy-BH co-evolution scenario. Stars represent our 11 DSFGs and are colour-coded by galaxy age (i.e. $\tau_\star$). We note that they match the model prediction within 2σ, again witnessing that the main drivers of the evolution of our 11 DSFGs can be traced back mostly to *in situ* processes. The superimposed grey symbols represent the median values found by da Cunha et al. (2015), Casey et al. (2017), Franco

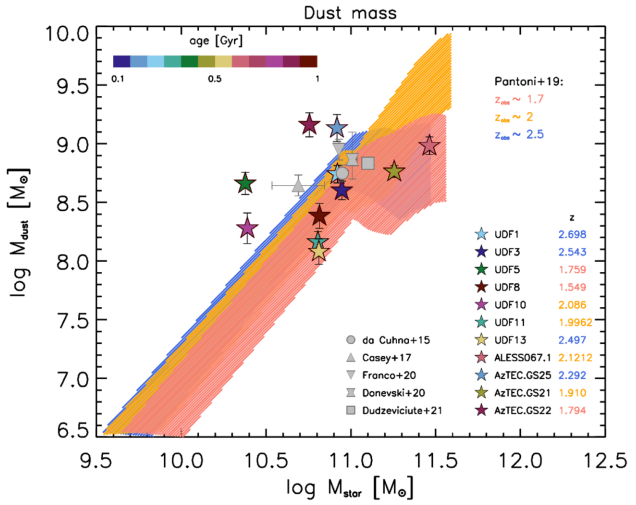

Figure 4. Statistical relationship between dust mass $M_{\rm dust}$ and stellar mass $M_\star$ for the high-z star-forming progenitors of ETGs by Pantoni et al. (2019) at three different observational redshifts: $z \sim 1.5$ (red), ~ 2 (orange), and ~ 2.5 (blue), with its 1σ scatter (shaded area). Stars represent the outcomes for the 11 DSFGs of our sample derived from SED fitting as explained in Section 4.2 and corrected following Magdis et al. (2012). Symbols are colour-coded by galaxy age (i.e. $\tau_\star$). Galaxy redshift is indicated in the legend next to galaxy ID and colour-coded by the corresponding redshift bin. Grey symbols represent the median values obtained by some other existing samples of high-z DSFGs, as specified in the legend.

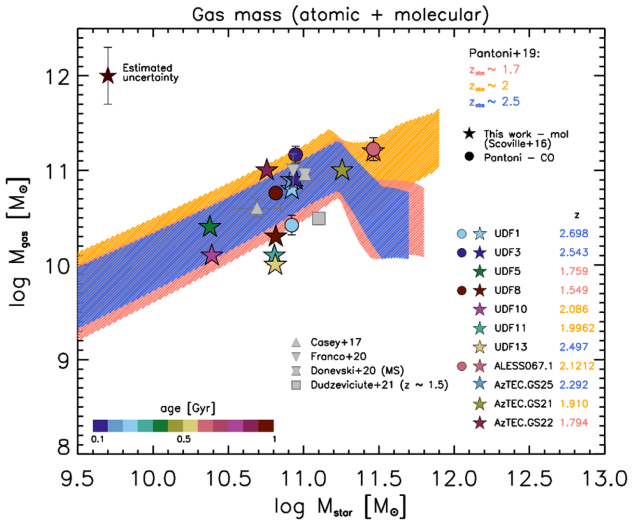

Figure 5. Statistical relationship between gas mass $M_{\rm gas}$ and stellar mass $M_\star$ for the high-z star-forming progenitors of ETGs by Pantoni et al. (2019) at three different observational redshifts: $z \sim 1.5$ (red), ~ 2 (orange), and ~ 2.5 (blue), with its 1σ scatter (shaded area). Stars represent the outcomes for the 11 DSFGs of our sample derived from SED fitting as explained in Section 4.3, following the approach by Scoville et al. (2016). The estimated uncertainty ($\sim$0.3 dex) is consistent with the 1σ scatter of the relation and is shown in the top left-hand corner of the plot. Circles stand for the H_2 masses estimated from $J > 1$ CO lines by and by Pantoni et al. (in preparation). Symbols are colour-coded by galaxy age (i.e. $\tau_\star$). Galaxy redshift is indicated in the legend next to galaxy ID and colour-coded by the corresponding redshift bin. Grey symbols represent the median values obtained by some other existing samples of high-z DSFGs, as specified in the legend.

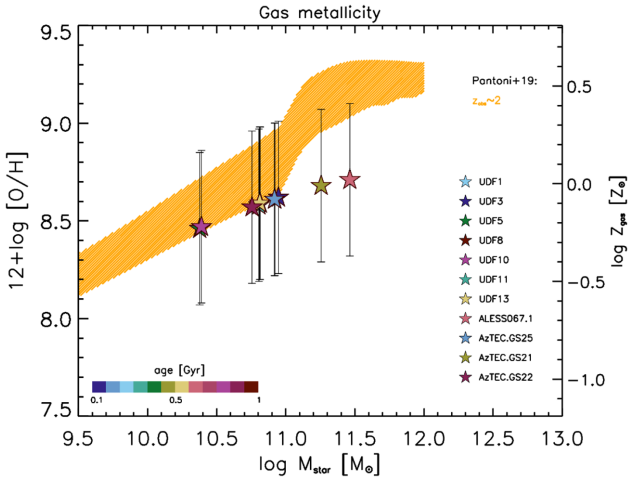

Figure 6. Statistical relationship between gas metallicity $Z_{\rm gas}$ and stellar mass $M_\star$ for high-z star-forming progenitors of ETGs, by Pantoni et al. (2019) at $z \sim 2$ (orange), with its 1σ scatter (shaded area). Stars represent our outcomes for the 11 DSFGs of our sample derived as explained in Section 4.3. Symbols are colour-coded by the galaxy age (i.e. $\tau_\star$).

et al. (2020), Donevski et al. (2020), and Dudzevičiūtė et al. (2021), as specified in the legend. The corresponding outcomes, found also for statistical samples of DSFGs in the photometric redshift range $0.5 < z_{\rm phot} < 5$ (see Donevski et al. 2020; Dudzevičiūtė et al. 2021), are in agreement with both the model predictions by Pantoni et al. (2019) and the corresponding median values of our sample, i.e. $M_{\rm dust} \sim 4.6 \times 10^8$ and $M_{\rm gas,\,mol} \sim 3.2 \times 10^{10}$ $M_\odot$ (cf. Table 13). It follows that our approach and selection criteria (see Section 2) do not introduce any substantial bias and may be applied to statistical samples of spectroscopically confirmed DSFGs, as soon as they will be available (see e.g. the ongoing z-GAL NOEMA Large Program 1; PIs: P. Cox; T. Bakx; H. Dannerbauer). In the following, we briefly comment on our outcomes, going into more details.

We derived the dust masses of our DSFGs, shown in Fig. 4, as described in Section 4.2. Then, we corrected the outcomes by a factor of 2 following Magdis et al. (2012). All the galaxies have a very high content of interstellar dust ($M_{\rm dust} > 10^8$ $M_\odot$), which is almost consistent with the relations by Pantoni et al. (2019), who predict a very rapid ($\sim 10^7$–10^8 yr) pollution of the ambient by dust and metals. We note that the interstellar dust content does not show any significant trend with galaxy age (i.e. the burst duration, $\tau_\star$). Four galaxies (UDF5, UDF10, AzTEC.GS25, AzTEC.GS22) are outliers (but still consistent with the statistical relation within 2σ): Although they are very close to galaxy main sequence at the corresponding redshift (cf. Fig. 3), they show a dust-to-stellar mass ratio very similar to that of ALMA starbursts in the sample studied by Donevski et al. (2020), i.e. $M_{\rm dust}/M_\star \gtrsim 0.01$. It could indicate that they are experiencing a quicker growth of dust in their ISM (on time-scales shorter than 10^8 yr), or that they are characterized by much longer dust destruction time-scales, preserving larger grains longer (see Donevski et al. 2020, their section 4).

In Fig. 5, we compare the molecular gas mass estimates for our 11 DSFGs (stars and circles, colour-coded by galaxy age, i.e. $\tau_\star$) with the predictions by Pantoni et al. (2019, coloured shaded area, including their 1σ scatter, for three redshift bins spanning the sample redshift range) and the median values recently found by some studies of high-z DSFGs exploiting SED fitting (i.e. Casey et al. 2017; Donevski et al. 2020; Franco et al. 2020; Dudzevičiūtė et al. 2021, grey symbols). We find them in great accordance, within the errors. No significant

trend emerges, neither in redshift or galaxy age. Stars represent our molecular gas mass estimates that we derived from dust FIR continuum following the approach by Scoville et al. (2016), as described in Section 4.3. Error bars, shown in the top left-hand corner of Fig. 5, are comparable to the 1σ scatter of the statistical relationships by Pantoni et al. (2019). Even if the latter predicts the evolution of the total gas mass, i.e. HI + H_2, with galaxy stellar mass (at a given redshift), comparing the two is still valid since we expect the molecular phase to be definitely dominant for these objects. Circles represent the estimates for the hydrogen molecular mass derived from $J > 1$ CO lines (Pantoni et al., in preparation; see the discussion in Section 4.3), which are listed in Table 7 and available for four galaxies, i.e. UDF1, UDF3, UDF8 and ALESS067.1. We derived the H_2 masses by assuming an $\alpha_{CO} = 3.6\ M_\odot(K\ km\ s^{-1}\ pc^2)^{-1}$ (see the discussion in Section 4.3), consistently with the approach followed by Scoville et al. (2016). The outcomes are almost in agreement within the error bars (the comparison is sensible as H_2 constitutes the large majority of the molecular gas content in galaxies: Even when corrected for helium mass by a factor of 1.36, the estimations are still consistent). However, some differences can be traced back to the fact that dust and CO emission often sample diverse (more compact/extended) galaxy regions, respectively (see e.g. Carilli & Walter 2013; Scoville et al. 2014, 2016, 2017; Elbaz et al. 2018).

All the galaxies have almost solar metallicities (even if error bars are huge; see Fig. 6), and do not show any significant trend with galaxy age. We compare the gas metallicity just with the statistical relation by Pantoni et al. (2019) at $z \sim 2$, since it does not show a significant evolution in redshift and the gas metallicity of our DSFGs is not strictly constrained due to the big uncertainties, i.e. ∼0.4 dex.

The large content of cold gas ($10^{10} \lesssim M_{gas,mol}/M_\odot \lesssim 10^{11}$), interstellar dust ($M_{dust} > 10^8\ M_\odot$), and stars ($3 \times 10^{10} \lesssim M_\star/M_\odot \lesssim 3 \times 10^{11}$), associated with relatively short depletion time-scales (∼200 Myr) and compact sizes in the ALMA continuum ($r_{ALMA} \lesssim 2$ kpc) suggest that our 11 DSFGs are the high-z star-forming progenitors of (compact) massive elliptical galaxies, caught in the *compaction phase*, i.e. a phase characterized by clump/gas migration toward the galaxy centre, where the intense dust-enshrouded star formation takes place and most of the stellar mass is accumulated (see Lapi et al. 2018). This statement is furthermore confirmed by the detection of an X-ray emitting AGN for the majority of DSFGs in our sample (Section 4.4), which does not emerge in the radio domain. Indeed, while the star formation ignites in the host galaxy, the *in situ* scenario predicts the growth of the central BH to occur at mild super-Eddington rates so that rotational energy cannot be easily funnelled into jets to power radio emission: The AGN is expected to be radio-silent and to shine as an X-ray source. This is possibly the case of the objects in our sample that are located to the upper left-hand side of galaxy main sequence (cf. Fig. 3). Then, following the *in situ* scenario, we expect AGN X-ray luminosity to overwhelm that associated with star formation, becoming clearly detectable at luminosities $L_X \gtrsim 10^{42}$ erg s^{-1} (cf. Fig. 2: Most of our DSFGs have $L_X > 10^{42}$). AGN power progressively increases to values similar to or even exceeding that of star formation in the host galaxy, originating outflows that can quench star formation in the host galaxy by heating and removing interstellar gas and dust from the ISM (i.e. AGN energy/momentum feedback). Still, these jets (that are driven by thin disc accretion) are rather ineffective in producing radio emission so that the AGN is radio-quiet and does not emerge clearly from the host galaxy emission in the radio domain (see Mancuso et al. 2017, and references therein). This must be the case of the galaxies that perfectly overlap the galaxy main sequence at the corresponding redshift (cf. Fig. 3). For a few objects we found the radio emission to be more extended than the FIR one, possibly being a signature of the forthcoming AGN feedback (e.g. UDF11; see Rujopakarn et al. 2016). AGN feedback can be associate also to the broad ($\Delta v \sim 500$ km s^{-1}), double-peaked CO emission-line profile observed for UDF3, UDF8 and ALESS067.1, which may indicate the presence of a molecular outflow. However, we need higher resolution images to provide the right interpretation of this evidence, which is also consistent with a rotating disc of molecular gas (i.e. unresolved; Pantoni et al., in preparation). Finally, as a consequence of AGN feedback, we expect star formation to be abruptly quenched: afterwards stellar populations evolve passively and the galaxy must become a red and dead ETG.

Also the recent outcomes by Stacey et al. (2020), studying seven gravitationally lensed quasars at $z = 1.5$–2.8, support the AGN evolution as depicted by *in situ* galaxy-BH co-evolution scenario. Interestingly, the new finding by Rizzo et al. (2020) of a massive ($M_\star \simeq 1.2 \times 10^{10}\ M_\odot$) rotationally supported ($v/\sigma = 9.7 \pm 0.4$) IR-luminous ($L_{IR} = (2.4 \pm 0.4) \times 10^{12}\ L_\odot$) galaxy at $z \sim 4.2$, experiencing an intense episode of star-formation (SFR $=352 \pm 65\ M_\odot\ yr^{-1}$ and $\tau_{depl} = 38 \pm 9$ Myr), is in perfect alignment with the aforementioned scenario and with its prediction on galaxy kinematics, witnessing that the main channels of such a strong and dusty star formation activity must be *in situ*. Indeed, if the star-forming burst had been triggered by high-z wet merging events, we would have expected the galaxy to be dynamically hot, chaotic and strongly unstable: e.g. the most recent cosmological magneto-hydrodynamical simulation TNG50 gives $v/\sigma < 3$ for those values of stellar mass and redshift (Pillepich et al. 2019). Recently, an increasing number of studies on $z \sim 2$ massive star-forming galaxy kinematics have recognized the interaction/merging triggered bursts not to dominate DSFG population (e.g. Förster Schreiber et al. 2006, 2011). A similar result is found by cosmological simulations, showing that the merger rate at the peak of Cosmic SFH (i.e. $z \sim 2$, corresponding to a cosmic time of ∼3 Gyr) is too small to explain alone the abundant population of DSFGs observed at that epoch (e.g. Dekel et al. 2009; Stewart et al. 2009; Hopkins & Hernquist 2010; Rodriguez-Gomez et al. 2016).

Although these pieces of evidence concurrently suggest that the main mechanisms leading high-z DSFG evolution can be mostly ascribed to local, *in situ* condensation processes and our results vastly support this scenario; certainly mergings and galaxy interactions play a role in determining the evolution of galaxies, especially in galaxy (proto-)clusters and densely populated environments (e.g. Tadaki et al. 2019).

In a forthcoming paper (Pantoni et al., in preparation), we will provide a refinement of the analysis by focusing on the ALMA view of the sample and using additional information collected from literature, such as multiwavelength images from public catalogues. Any evidence of interaction/merging, as well as any signature of AGN feedback, will be then included in the final picture.

6 SUMMARY AND CONCLUSIONS

We have presented a panchromatic study of 11 DSFGs at the peak of Cosmic SFH, which we selected in the (sub-)millimetre regime requiring the following criteria to be fulfilled for each galaxy: three or more detections in the optical domain ($\lambda_{obs} = 0.3$–1 μm); six or more detections in the NIR+MIR bands ($\lambda_{obs} = 1$–25 μm); two or more detections in the FIR band ($\lambda_{obs} = 25$–400 μm); spectroscopically confirmed redshift in the range $1.5 < z_{spec} < 3$; and one or more detections and/or upper limits in the radio and X-ray regimes.

The sources are located in one of the deepest multiband field currently available, the GOODS-S. We exploited the extensive multiwavelength photometry, from the X-ray to the radio band, to reliably re-construct and precisely model galaxy SED, by using a physically motivated modelling of stellar light attenuation by dust. We used CIGALE to extract the main astrophysical properties of our DSFGs (e.g. SFR, stellar mass, stellar attenuation law by dust, dust temperature, IR luminosity) from their SEDs. We exploited the R-J dust continuum to estimate galaxy dust mass ($M_{\rm dust}$) and, when CO spectroscopy was not available, their gas mass (total $M_{\rm gas,\,tot}$ and molecular $M_{\rm gas,\,mol}$). Finally, we took advantage of the X-ray and radio photometry to guess the presence of an AGN. In the following, we summarize our main findings:

(i) The 11 DSFGs of our sample are (almost) main-sequence objects, with a median $M_\star = 6.5 \times 10^{10}$ M$_\odot$ and SFR $\sim$250 M$_\odot$ yr^{-1}. They are experiencing an intense and dusty (median $L_{\rm IR} \sim 2 \times 10^{12}$ $L_\odot$) burst of star formation, with typical duration $\tau_\star$ ranging between 0.2 and 1 Gyr. Despite their young age, the interstellar dust content is high ($M_{\rm dust} > \times 10^8$ M$_\odot$), possibly due to a very rapid enrichment of the ISM (on typical time-scales of 10^7–10^8 yr). The gas mass (median $M_{\rm gas,\,tot} \sim 6 \times 10^{10}$ and $M_{\rm gas,\,mol} \sim 3 \times 10^{10}$ M$_\odot$), fuelling the dusty star formation, will be rapidly depleted, over a median time-scale $\tau_{\rm depl} \sim 200$ Myr. Out of 11 objects, 9 have an X-ray luminous ($L_{\rm 2-10\,keV} \gtrsim 10^{42}$ erg s^{-1}) counterpart in the *Chandra* $\simeq$ 7-Ms catalogue and two of them are clearly dominated by the active nucleus emission ($L_{\rm 2-10\,keV} \gtrsim 10^{43}$–$10^{44}$ erg s^{-1}). The radio luminosity is consistent with the emission coming from galaxy star formation, suggesting that the AGN, if present, should be radio-silent or quiet.

(ii) We interpret our outcomes in light of the *in situ* galaxy-BH co-evolution scenario (see e.g. Mancuso et al. 2016a,b; Mancuso et al. 2017; Shi et al. 2017; Lapi et al. 2018), which provides a possible consistent picture of high-z DSFG formation and evolution. In particular we compare our results with the predictions by the analytic model presented in Pantoni et al. (2019), describing the spatially averaged time evolution of the gas, dust, stellar and metals content in high-z star-forming counterparts of local ETGs, following the prescriptions by the aforementioned *in situ* scenario. We find our outcomes to match the model predictions within their 2σ scatter, suggesting that the main drivers of the evolution of our 11 DSFGs can be traced back mostly to local condensation processes.

(iii) We complemented these results by exploiting multiwavelength images from public catalogues, which allowed us to include in our final interpretation every signature of galaxy merging/interactions and feedback. The compact FIR and radio sizes ($\lesssim$a few kpc) of our DSFGs, together with their optical radii ($\sim$2–6 kpc), suggest that the bulk of their star formation can be traced back to *in situ* condensation processes. Most of our sources shows an optical isolated morphology, while four galaxies (UDF11, ALESS067.1, AzTEC.GS21, AzTEC.GS22) have more complex (i.e. clumpy) morphologies, possibly indicating the presence of minor companions – that can prolong the star formation in the dominant galaxy by refuelling it with gas – or just being a signature of the ongoing dusty star formation. Higher resolution imaging are needed to definitely clarify the picture. However, we do not expect these interactions to have an important impact on the subsequent evolution of the dominant galaxy.

(iv) Following the predictions by the *in situ* galaxy-BH co-evolution (see Lapi et al. 2018), we can state that the majority of the galaxies in our sample is caught in the compaction phase and we expect them to be quenched by the AGN feedback in $\lesssim 10^8$ yr. For four objects, we found some signatures of AGN feedback either in the radio band (UDF11), which appears more extended than the FIR one, or by the detection of possible AGN-driven molecular outflows (UDF3, UDF8, ALESS067.1). We expect their subsequent evolution to be passive, mainly driven by their stellar populations aging and mass additions by dry merger events, and ultimately to become compact quiescent galaxies or massive ETGs. In a forthcoming paper (focusing on the ALMA view of the sample; Pantoni et al., in preparation) we will gathered together all these evidences in order to provide a novel approach in characterizing the individual DSFG and predicting its subsequent evolution.

(v) We have compared the results obtained for our sample of 11 spectroscopically confirmed $z \sim 2$ DSFGs with other recent good studies on high-z DSFGs exploiting SED fitting, and we find a great agreement between the median values of the main physical quantities estimated for these galaxies, such as stellar mass, gas mass and dust mass. Thus, we can conclude that our approach and selection criteria do not introduce any substantial bias and may be applied to statistical samples of spectroscopically confirmed DSFGs, as soon as they will be available (see e.g. the ongoing z-GAL NOEMA Large Program; PIs: P. Cox; T. Bakx; H. Dannerbauer).

(vi) Finally, we would highlight the importance of combining multiband photometry, gas spectroscopy, and high-resolution imaging with a physically motivated model in order to characterize the role of high-z DSFGs in the context of galaxy formation and evolution and the impact of galaxy interactions and AGN feedback in determining their evolution.

ACKNOWLEDGEMENTS

The authors thank the anonymous referee for stimulating and constructive comments that helped to improve this study. LP gratefully thanks S. Campitiello for the helpful discussions.

This paper makes use of the following ALMA data: ADS/JAO.ALMA#2011.0.00294.S (PI: Smail); #2012.1.00983.S (PI: Leiton); #2012.1.00173.S (PI: Dunlop); #2015.1.00098.S (PI: Kohno); #2015.1.00543.S (PI: Elbaz); #2015.1.00948.S (PI: da Cunha); #2015.1.01074.S (PI: Inami); #2015.1.00242.S and #2016.1.01079.S (PI: Bauer); #2016.1.00564.S (PI: Weiss); and #2017.1.01347.S (PI: Pope). ALMA is a partnership of ESO (representing its member states), NSF (USA), and NINS (Japan), together with NRC (Canada), NSC and ASIAA (Taiwan), and KASI (Republic of Korea), in cooperation with the Republic of Chile. The Joint ALMA Observatory is operated by ESO, AUI/NRAO, and NAOJ. We acknowledge financial support from the grants: PRIN MIUR 2017 prot. 20173ML3WW 001 and PRIN MIUR 2017 prot. 20173ML3WW 002 ('Opening the ALMA window on the cosmic evolution of gas, stars and massive black holes'). AL is supported by the EU H2020-MSCAITN-2019 Project 860744 'BiD4BEST: Big Data applications for Black hole Evolution STudies'.

DATA AVAILABILITY

This paper uses public data products from ALMA Archive (repository available at the following link: https://almascience.nrao.edu/asax/; note that project codes of interest are listed in the Acknowledgements).

Photometric optical, infrared, radio, and X-ray data come from (in the order) the following:

(i) GOODS-MUSIC sample: a multicolour catalogue of near-IR selected galaxies in the GOODS-South field (Grazian et al. 2006a,

available at the link: https://cdsarc.unistra.fr/viz-bin/cat/J/A+A/449/951; VizieR DOI: 10.26093/cds/vizier.34490951);

(ii) combined PEP/GOODS-Herschel data of the GOODS fields by Magnelli et al. (2013) at the link https://www.mpe.mpg.de/ir/Research/PEP/DR1 and publicly available at http://www.mpe.mpg.de/ir/Research/PEP/public_data_releases.php (see also Magnelli et al. 2011a, available at the link: https://cdsarc.unistra.fr/viz-bin/cat/J/A+A/528/A35; VizieR DOI: 10.26093/cds/vizier.35280035);

(iii) Herschel Multi-tiered Extragalactic Survey: HerMES (Oliver et al. 2014; Hermes Team et al. 2017, publicly available through the Herschel Database in Marseille, HeDaM, at http://hedam.oamp.fr/HerMES and at the VizieR links https://cdsarc.unistra.fr/viz-bin/cat/VIII/95 and https://cdsarc.unistra.fr/viz-bin/cat/VIII/103);

(iv) Very Large Array 1.4-GHz survey of the Extended Chandra Deep Field South: second data release (Miller et al. 2013a, available at the link: https://cdsarc.unistra.fr/viz-bin/cat/J/ApJS/205/13; VizieR DOI: 10.26093/cds/vizier.22050013);

(v) Very Large Array 6-GHz imaging by Rujopakarn et al. (2016) (follow-up of the B6 ALMA sources by Dunlop et al. 2017, in the HUDF-S; project ID ADS/JAO.ALMA#2012.1.00173.S): project ID VLA/14A-360.

(vi) Chandra Deep Field-South survey: 7-Ms source catalogues (Luo et al. 2017a, available at the VizieR link: https://cdsarc.unistra.fr/viz-bin/cat/J/ApJS/228/2).

REFERENCES

Aird J. et al., 2010, MNRAS, 401, 2531
Asmus D., Gandhi P., Hönig S. F., Smette A., Duschl W. J., 2015, MNRAS, 454, 766
Banday A. J., Wolfendale A. W., 1991, MNRAS, 248, 705
Barro G. et al., 2013, ApJ, 765, 104
Barro G. et al., 2016a, ApJ, 820, 120
Barro G. et al., 2016b, ApJ, 827, L32
Barrufet L. et al., 2020, A&A, 641, A129
Beckwith S. V. W. et al., 2006, AJ, 132, 1729
Berta S., Lutz D., Genzel R., Förster-Schreiber N. M., Tacconi L. J., 2016, A&A, 587, A73
Béthermin M. et al., 2014, A&A, 567, A103
Béthermin M. et al., 2017, A&A, 607, A89
Bianchi S., 2013, A&A, 552, A89
Bianchini F., Fabbian G., Lapi A., Gonzalez-Nuevo J., Gilli R., Baccigalupi C., 2019, ApJ, 871, 136
Blain A. W., Smail I., Ivison R. J., Kneib J.-P., Frayer D. T., 2002, Phys. Rep., 369, 111
Bonzini M., Padovani P., Mainieri V., Kellermann K. I., Miller N., Rosati P., Tozzi P., Vattakunnel S., 2013, MNRAS, 436, 3759
Boquien M., Burgarella D., Roehlly Y., Buat V., Ciesla L., Corre D., Inoue A. K., Salas H., 2019, A&A, 622, A103
Bruzual G., Charlot S., 2003, MNRAS, 344, 1000
Buat V., Ciesla L., Boquien M., Małek K., Burgarella D., 2019, A&A, 632, A79
Calura F. et al., 2017, MNRAS, 465, 54
Calzetti D., Armus L., Bohlin R. C., Kinney A. L., Koornneef J., Storchi-Bergmann T., 2000, ApJ, 533, 682
Carilli C. L., Walter F., 2013, ARA&A, 51, 105
Casey C. M. et al., 2017, ApJ, 840, 101
Casey C. M. et al., 2018, ApJ, 862, 77
Casey C. M., 2012, MNRAS, 425, 3094
Casey C. M., Chapman S. C., Smail I., Alaghband -Zadeh S., Bothwell M. S., Swinbank A. M., 2011, MNRAS, 411, 2739
Casey C. M., Narayanan D., Cooray A., 2014, Phys. Rep., 541, 45
Cassarà L. P. et al., 2016, A&A, 593, A9
Chabrier G., 2003, PASP, 115, 763
Chapin E. L. et al., 2011, MNRAS, 411, 505
Chapman S. C., Windhorst R., Odewahn S., Yan H., Conselice C., 2003, ApJ, 599, 92
Chapman S. C., Blain A. W., Smail I., Ivison R. J., 2005, ApJ, 622, 772
Ciesla L., Elbaz D., Fensch J., 2017, A&A, 608, A41
Cimatti A. et al., 2008, A&A, 482, 21
Citro A., Pozzetti L., Moresco M., Cimatti A., 2016, A&A, 592, A19
Condon J. J., 1992, ARA&A, 30, 575
Cowie L. L., González-López J., Barger A. J., Bauer F. E., Hsu L.-Y., Wang W.-H., 2018, ApJ, 865, 106
D'Amato Q. et al., 2020, A&A, 636, A37
da Cunha E. et al., 2015, ApJ, 806, 110
Daddi E. et al., 2007, ApJ, 670, 156
Daddi E. et al., 2010, ApJ, 713, 686
Daddi E. et al., 2015, A&A, 577, A46
Dale D. A. et al., 2012, ApJ, 745, 95
Decarli R. et al., 2016, ApJ, 833, 70
Dekel A. et al., 2009, Nature, 457, 451
Dekel A., Birnboim Y., 2006, MNRAS, 368, 2
Delvecchio I. et al., 2014, MNRAS, 439, 2736
Dickinson M., GOODS Legacy Team, 2001, AAS Meeting Abstracts #198, p. 25.01
Donevski D. et al., 2018, A&A, 614, A33
Donevski D. et al., 2020, A&A, 644, A144
Draine B. T., 2011, in Spergel D. N., ed., Physics of the Interstellar and Intergalactic Medium. Princeton University Press, Princeton and Oxford, p. 92
Draine B. T., Li A., 2007, ApJ, 657, 810
Dudzevičiūtė U. et al., 2021, MNRAS, 500, 942
Dunlop J. S. et al., 2017, MNRAS, 466, 861
Dye S. et al., 2015, MNRAS, 452, 2258
Eales S. et al., 2010, PASP, 122, 499
Eales S., de Vis P., Smith M. W. L., Appah K., Ciesla L., Duffield C., Schofield S., 2017, MNRAS, 465, 3125
Eke V., Efstathiou G., Wright L., 2000, MNRAS, 315, L18
Elbaz D. et al., 2018, A&A, 616, A110
Fall S. M., 2002, in Athanassoula E., Bosma A., Mujica R., eds, ASP Conf. Ser. Vol. 275, Discs of Galaxies: Kinematics, Dynamics and Peturbations. Astron. Soc. Pac., San Francisco, p. 389
Feltre A., Hatziminaoglou E., Fritz J., Franceschini A., 2012, MNRAS, 426, 120
Forrest B. et al., 2018, ApJ, 863, 131
Förster Schreiber N. M. et al., 2006, ApJ, 645, 1062
Förster Schreiber N. M. et al., 2011, ApJ, 739, 45
Franco M. et al., 2018, A&A, 620, A152
Franco M. et al., 2020, A&A, 643, A30
Fritz J., Franceschini A., Hatziminaoglou E., 2006, MNRAS, 366, 767
Fujimoto S., Ouchi M., Shibuya T., Nagai H., 2017, ApJ, 850, 83
Gandhi P., Horst H., Smette A., Hönig S., Comastri A., Gilli R., Vignali C., Duschl W., 2009, A&A, 502, 457
Genzel R. et al., 2012, ApJ, 746, 69
Giavalisco M. et al., 2004, ApJ, 600, L93
Gilli R. et al., 2014, A&A, 562, A67
Grazian A. et al., 2006a, VizieR Online Data Catalog, p. J/A+A/449/951
Grazian A. et al., 2006b, A&A, 449, 951
Gruppioni C. et al., 2013, MNRAS, 432, 23
Gruppioni C. et al., 2020, A&A, 643, A8
Harrison C. M. et al., 2016, MNRAS, 457, L122
Hatsukade B. et al., 2018, PASJ, 70, 105
Hermes Team et al., 2017, VizieR Online Data Catalog, p. VIII/103
Hildebrand R. H., 1983, QJRAS, 24, 267
Hodge J. A. et al., 2013, ApJ, 768, 91
Hodge J. A. et al., 2019, ApJ, 876, 130
Hodge J. A., da Cunha E., 2020, Royal Society Open Science, 7, 12
Hopkins P. F., Hernquist L., 2010, MNRAS, 402, 985
Hopkins P. F., Somerville R. S., Hernquist L., Cox T. J., Robertson B., Li Y., 2006, ApJ, 652, 864
Ibar E., Ivison R. J., Biggs A. D., Lal D. V., Best P. N., Green D. A., 2009, MNRAS, 397, 281

Ibar E., Ivison R. J., Best P. N., Coppin K., Pope A., Smail I., Dunlop J. S., 2010, MNRAS, 401, L53
Ikarashi S. et al., 2015, ApJ, 810, 133
Ishibashi W., Courvoisier T. J. -L., 2010, A&A, 512, A58
Kellermann K. I., 1966, ApJ, 146, 621
Kennicutt R. C., Evans N. J., 2012, ARA&A, 50, 531
Kewley L. J., Ellison S. L., 2008, ApJ, 681, 1183
Kriek M. et al., 2006, ApJ, 649, L71
Kriek M. et al., 2007, ApJ, 669, 776
Kurk J. et al., 2013, A&A, 549, A63
Lapi A. et al., 2018, ApJ, 857, 22
Lehmer B. D. et al., 2016, ApJ, 825, 7
Leja J., Johnson B. D., Conroy C., van Dokkum P. G., Byler N., 2017, ApJ, 837, 170
Leroy A. K. et al., 2011, ApJ, 737, 12
Liang L. et al., 2019, MNRAS, 489, 1397
Liu D. et al., 2019, ApJS, 244, 40
Lo Faro B., Buat V., Roehlly Y., Alvarez-Marquez J., Burgarella D., Silva L., Efstathiou A., 2017, MNRAS, 472, 1372
Luo B. et al., 2017a, VizieR Online Data Catalog, p. J/ApJS/228/2
Luo B. et al., 2017b, ApJS, 228, 2
Lutz D. et al., 2011, A&A, 532, A90
Madau P., Dickinson M., 2014, ARA&A, 52, 415
Magdis G. E. et al., 2012, ApJ, 760, 6
Magnelli B. et al., 2013, A&A, 553, A132
Magnelli B., Elbaz D., Chary R. R., Dickinson M., Le Borgne D., Frayer D. T., Willmer C. N. A., 2011a, VizieR Online Data Catalog, p. J/A+A/528/A35
Magnelli B., Elbaz D., Chary R. R., Dickinson M., Le Borgne D., Frayer D. T., Willmer C. N. A., 2011b, A&A, 528, A35
Małek K. et al., 2018, A&A, 620, A50
Mancuso C. et al., 2017, ApJ, 842, 95
Mancuso C., Lapi A., Shi J., Gonzalez-Nuevo J., Aversa R., Danese L., 2016a, ApJ, 823, 128
Mancuso C., Lapi A., Shi J., Cai Z. Y., Gonzalez-Nuevo J., Béthermin M., Danese L., 2016b, ApJ, 833, 152
Martis N. S., Marchesini D. M., Muzzin A., Stefanon M., Brammer G., da Cunha E., Sajina A., Labbe I., 2019, ApJ, 882, 65
Massardi M. et al., 2018, A&A, 610, A53
Michałowski M., Hjorth J., Watson D., 2010, A&A, 514, A67
Miettinen O. et al., 2015, A&A, 577, A29
Miller N. A. et al., 2013a, VizieR Online Data Catalog, p. J/ApJS/205/13
Miller N. A. et al., 2013b, ApJS, 205, 13
Momcheva I. G. et al., 2016, ApJS, 225, 27
Mor R., Netzer H., Trakhtenbrot B., Shemmer O., Lira P., 2012, ApJ, 749, L25
Moustakas J. et al., 2013, ApJ, 767, 50
Mullaney J. R. et al., 2012, MNRAS, 419, 95
Mullaney J. R., Alexander D. M., Goulding A. D., Hickox R. C., 2011, MNRAS, 414, 1082
Murphy E. J. et al., 2011, ApJ, 737, 67
Murphy E. J. et al., 2012, ApJ, 761, 97
Narayanan D., Conroy C., Davé R., Johnson B. D., Popping G., 2018, ApJ, 869, 70
Negrello M. et al., 2014, MNRAS, 440, 1999
Nenkova M., Sirocky M. M., Ivezić, Ž., Elitzur M., 2008, ApJ, 685, 147
Neri R. et al., 2020, A&A, 635, A7
Nguyen H. T. et al., 2010, A&A, 518, L5
Noeske K. G. et al., 2007, ApJ, 660, L43
Oliver S. J. et al., 2012, MNRAS, 424, 1614
Oliver S. J. et al., 2014, VizieR Online Data Catalog, p. VIII/95
Oteo I. et al., 2016, ApJ, 827, 34
Oteo I., Zwaan M. A., Ivison R. J., Smail I., Biggs A. D., 2016, ApJ, 822, 36
Padovani P., Bonzini M., Kellermann K. I., Miller N., Mainieri V., Tozzi P., 2015, MNRAS, 452, 1263
Page M. J. et al., 2012, Nature, 485, 213
Pantoni L., Lapi A., Massardi M., Goswami S., Danese L., 2019, ApJ, 880, 129
Papovich C., Finkelstein S. L., Ferguson H. C., Lotz J. M., Giavalisco M., 2011, MNRAS, 412, 1123
Pearson W. J. et al., 2018, A&A, 615, A146
Pillepich A. et al., 2019, MNRAS, 490, 3196
Planck Collaboration et al., 2020, A&A, 641, A6
Popesso P. et al., 2009, A&A, 494, 443
Pozzi F. et al., 2012, MNRAS, 423, 1909
Pozzi F., Calura F., Zamorani G., Delvecchio I., Gruppioni C., Santini P., 2020, MNRAS, 491, 5073
Ranalli P. et al., 2013, A&A, 555, A42
Ranalli P., Comastri A., Setti G., 2003, A&A, 399, 39
Renzini A., 2006, ARA&A, 44, 141
Riechers D. A. et al., 2014, ApJ, 796, 84
Rizzo F., Vegetti S., Powell D., Fraternali F., McKean J. P., Stacey H. R., White S. D. M., 2020, Nature, 584, 201
Rodighiero G. et al., 2011, ApJ, 739, L40
Rodriguez-Gomez V. et al., 2016, MNRAS, 458, 2371
Romanowsky A. J., Fall S. M., 2012, ApJS, 203, 17
Rosario D. J. et al., 2012, A&A, 545, A45
Rujopakarn W. et al., 2016, ApJ, 833, 12
Salim S., Boquien M., Lee J. C., 2018, ApJ, 859, 11
Salmon B. et al., 2016, ApJ, 827, 20
Santini P. et al., 2014, A&A, 562, A30
Schreiber C., Elbaz D., Pannella M., Ciesla L., Wang T., Franco M., 2018, A&A, 609, A30
Schurer A., Calura F., Silva L., Pipino A., Granato G. L., Matteucci F., Maiolino R., 2009, MNRAS, 394, 2001
Scoville N. et al., 2014, ApJ, 783, 84
Scoville N. et al., 2016, ApJ, 820, 83
Scoville N. et al., 2017, ApJ, 837, 150
Shankar F., Weinberg D. H., Miralda-Escudé J., 2009, ApJ, 690, 20
Shi J., Lapi A., Mancuso C., Wang H., Danese L., 2017, ApJ, 843, 105
Simpson J. M. et al., 2014, ApJ, 788, 125
Simpson J. M. et al., 2015, ApJ, 807, 128
Smail I., Morrison G., Gray M. E., Owen F. N., Ivison R. J., Kneib J.-P., Ellis R. S., 1999, ApJ, 525, 609
Smit R., Bouwens R. J., Franx M., Illingworth G. D., Labbé I., Oesch P. A., van Dokkum P. G., 2012, ApJ, 756, 14
Speagle J. S., Steinhardt C. L., Capak P. L., Silverman J. D., 2014, ApJS, 214, 15
Stacey H. R. et al., 2020, MNRAS, 493, 5290
Steinhardt C. L. et al., 2014, ApJ, 791, L25
Stewart K. R., Bullock J. S., Barton E. J., Wechsler R. H., 2009, ApJ, 702, 1005
Straughn A. N. et al., 2009, AJ, 138, 1022
Swinbank A. M., Chapman S. C., Smail I., Lindner C., Borys C., Blain A. W., Ivison R. J., Lewis G. F., 2006, MNRAS, 371, 465
Szokoly G. P. et al., 2004, ApJS, 155, 271
Tacconi L. J. et al., 2018, ApJ, 853, 179
Tadaki K.-I. et al., 2015, ApJ, 811, L3
Tadaki K.-I. et al., 2019, ApJ, 876, 1
Tadaki K.-I. et al., 2020, ApJ, 901, 74
Talia M. et al., 2018, MNRAS, 476, 3956
Talia M., Cimatti A., Giulietti M., Zamorani G., Bethermin M., Faisst A., Le Fèvre O., Smolčić V., 2020, ApJ, 909, 23
Targett T. A. et al., 2013, MNRAS, 432, 2012
Thomson A. P. et al., 2014, MNRAS, 442, 577
Tingay S. J., de Kool M., 2003, AJ, 126, 723
Toft S. et al., 2014, ApJ, 782, 68
Trayford J. W., Schaye J., 2019, MNRAS, 485, 5715
van der Wel A. et al., 2012, ApJS, 203, 24
van Dokkum P. G. et al., 2008, ApJ, 677, L5
Vanzella E. et al., 2008, A&A, 478, 83
Vattakunnel S. et al., 2012, MNRAS, 420, 2190
Walter F. et al., 2012, Nature, 486, 233
Wang R. et al., 2013, ApJ, 773, 44
Williams C. C. et al., 2019, ApJ, 884, 154
Willott C. J., Bergeron J., Omont A., 2015, ApJ, 801, 123

Windhorst R. A., Cohen S. H., 2010, in Whalen D. J., Bromm V., Yoshida N., eds, AIP Conf. Ser. Vol. 1294, First Stars and Galaxies: Challenges for the Next Decade. Am. Inst. Phys., New York, p. 225
Yun M. S. et al., 2012, MNRAS, 420, 957

APPENDIX A: DERIVATION OF INDIVIDUAL GALAXY ATTENUATION LAW

We derive the individual galaxy attenuation law (shown in Fig. 1, right-hand column), starting from stellar luminosities calculated by CIGALE. In particular, we describe how the two dust components (populating galaxy ISM and BCs) concurrently draw galaxy total attenuation law.

By definition, the attenuation law is a function of wavelength normalized to attenuation in the V (photometric) band, i.e. A_λ/A_V. Namely, a non-transparent medium along the line of sight (los) modify the source intrinsic monochromatic luminosity L^0_λ according to the law,

$$\frac{L_\lambda}{L^0_\lambda} = \mathrm{e}^{-\tau_\lambda}, \tag{A1}$$

where τ_λ is the medium optical depth and L_λ is the attenuated luminosity at a given λ. The attenuation at a given wavelength λ is then defined as

$$A_\lambda = -2.5 \log_{10} \frac{L_\lambda}{L^0_\lambda}. \tag{A2}$$

Comparing equations (A1) and (A2), it follows that $A_\lambda = 2.5 \log_{10}(e)\, \tau_\lambda = 1.086\, \tau_\lambda \simeq \tau_\lambda$.

We note that A_λ is actually a measure of the stellar luminosity that has been absorbed by dust, i.e. $\Delta L_\lambda = L^0_\lambda - L_\lambda$. In our case, $\Delta L^{\rm BC}_\lambda$, $\Delta L^{\rm ISM}_\lambda$, and $\Delta L^{\rm tot}_\lambda$ are provided by CIGALE for every galaxy in our sample, as outputs of SED fitting, together with stellar intrinsic luminosities, thus

$$A^{\rm i}_\lambda = -2.5 \log_{10} \frac{L^{0,\,i}_\lambda - \Delta L^{\rm i}_\lambda}{L^{0,\,i}_\lambda}, \tag{A3}$$

where i = BC, ISM, tot.

Attenuations in the V band (A^i_V) are obtained from equation (A3), taking the values corresponding to $\lambda = 5500$ Å. Then, deriving attenuation laws A^i_λ/A^i_V is straightforward.

APPENDIX B: DERIVATION OF GALAXY INTRINSIC 2–10 KEV LUMINOSITY

In the following, we convert the 0.5–7.0 keV luminosity by Luo et al. (2017b) into the corresponding 2–10 keV luminosity, given that the latter is the most widely used in literature to investigate galaxy evolution. We exploited the known intrinsic spectral index (≡1.8 or greater; Luo et al. 2017b) to estimate the conversion factor by using the X-ray simulator WebPIMMS,[7] the same tool used by Luo et al. (2017b) to obtain $N_{\rm H,int}$. Intrinsic and effective[8] spectral indices ($\Gamma_{\rm int}$ and $\Gamma_{\rm eff}$), together with $L_{0.5-7\,\rm keV} - L_{2-10\,\rm keV}$ conversion factors and the derived 2–10 keV intrinsic luminosities ($L_{2-10\,\rm keV}$), are listed in Table 9.

Then, we convert the 2–10 keV luminosities to be consistent with the redshift adopted in this work (cf. Table 1), not always exactly coincident with Luo et al. (2017b) ones. To this aim, we proceed as follows. If both the intrinsic X-ray luminosity $L_{\nu/(1+z)}$ of a source at a given redshift z and the power-law describing its X-ray emission are known, then it is possible to derive the corresponding observed flux $S_{\nu/(1+z)}$ applying the so-called *k-correction*. This correction is defined by the following equation:

$$S_{\nu/(1+z)} = (1+z)\, \frac{L_\nu}{L_{\nu/(1+z)}}\, \frac{L_{\nu/(1+z)}}{4\pi\, d_{\rm L}(z)^2}. \tag{B1}$$

Since $L_\nu \propto \nu^{-\alpha}$, with $\alpha > 0$ and $\Gamma = \alpha + 1 > 0$ (e.g. Ishibashi & Courvoisier 2010), where Γ is the energy spectral index, one can write

$$\frac{L_\nu}{L_{\nu/(1+z)}} = \left(\frac{\nu}{\nu/(1+z)}\right)^{-\alpha} = (1+z)^{-\alpha} = (1+z)^{1-\Gamma}.$$

This result, together with equation (B1), brings to

$$S_{\nu/(1+z)} = (1+z)^{2-\Gamma_{\rm int}}\, \frac{L_{\nu/(1+z)}}{4\pi\, d_{\rm L}(z)^2}, \tag{B2}$$

where $\Gamma_{\rm int}$ is the intrinsic energy spectral index, i.e. the one derived after the correction for an eventual intrinsic absorption. Specializing equation (B2) to our case, we have

$$S_{2-10\,\rm keV} = (1+z_{\rm L})^{2-\Gamma_{\rm int}}\, \frac{L_{2-10\,\rm keV}(z_{\rm L})}{4\pi\, d_{\rm L}(z_{\rm L})^2}, \tag{B3}$$

where $z_{\rm L}$ is the source redshift in Luo et al. (2017b). Then, exploiting equation (B3), it is possible to derive the observed flux $S_{2-10\,\rm keV}$ corresponding to the intrinsic luminosity $L_{2-10\,\rm keV}(z_{\rm L})$ provided by Luo et al. (2017b). Now, it is sufficient to invert equation (B2) with $S_{\nu/(1+z)} \equiv S_{2-10\,\rm keV}$, and from equation (B3), it follows

$$L_{\rm X,\,int} = (1+z_{\rm L})^{2-\Gamma_{\rm int}}\, \frac{L_{2-10\,\rm keV}(z_{\rm L})}{4\pi\, d_{\rm L}(z_{\rm L})^2}\, \frac{4\pi\, d_{\rm L}(z)^2}{(1+z)^{2-\Gamma_{\rm int}}}. \tag{B4}$$

Intrinsic 2–10 keV luminosities ($L_{\rm X,\,int}$) are listed in Table 9. The other quantities exploited to derive $L_{\rm X,\,int}$ are listed in Table B1.

[7] https://heasarc.gsfc.nasa.gov/cgi-bin/Tools/w3pimms/w3pimms.pl
[8] Note that the effective spectral index is actually almost coincident with the observed spectral index.

Table B1. In this table, we list IDs of the source associations (ID: this work; ID_X: G102) and their angular separation (d) in arcsec; redshifts adopted in this work (z) and the ones associated with X-ray sources in Luo et al. (2017b, z_L); intrinsic 0.5–7 keV luminosities from G102 ($L_{0.5-7\,keV}$); conversion factors (f_{conv}) from $L_{0.5-7\,keV}$ to $L_{2-10\,keV}$; 2–10 keV luminosities at redshift z_L ($L_{2-10\,keV}$); 2–10 keV intrinsic luminosities at redshift z (L_X); and effective spectral indices (Γ_{eff}) and the intrinsic ones (Γ_{int}).

ID	ID_X	d (arcsec)	z	z_L	$L_{0.5-7\,keV}$ (10^{42} erg s^{-1})	f_{conv}	$L_{2-10\,keV}$ (10^{42} erg s^{-1})	Γ_{eff}	Γ_{int}
UDF1	805	0.69	2.688	2.69	64.0	0.63	40.3	1.96	1.96
UDF3	718	0.54	2.544	2.547	4.6	0.40	1.8	2.44	2.44
UDF8	748	0.07	1.549	1.552	50.7	0.72	36.5	1.32	1.8
UDF10	756	0.31	2.086	2.096	2.7	0.22	0.6	3.0	3.0
UDF11	751	0.29	1.996	1.998	2.4	0.72	1.7	1.74	1.8
UDF13	655	0.26	2.497	2.07	2.3	0.57	1.3	2.07	2.07
ALESS067.1	794	0.40	2.1212	2.122	8.5	0.45	3.8	2.33	2.33
AzTEC.GS25	844	0.71	2.292	2.292	8.5	0.72	6.1	1.2	1.8
AzTEC.GS21	852	0.36	1.91	1.91	2.3	0.72	1.7	1.4	1.8

Note. In the last two columns, we show (in the order) the class (AGN or galaxy) associated with each source by Luo et al. (2017b) and the X-ray dominant component (active nucleus or host galaxy) found by our analysis.

This paper has been typeset from a TEX/LATEX file prepared by the author.